RSC Advances

PAPER

View Article Online
View Journal | View Issue

Check for updates

Cite this: *RSC Adv.*, 2017, **7**, 49720

TiO_2 nanotubes enriched with calcium, phosphorous and zinc: promising bio-selective functional surfaces for osseointegrated titanium implants

S. A. Alves, [ab] A. R. Ribeiro, [bcde] S. Gemini-Piperni, [bf] R. C. Silva, [c] A. M. Saraiva, [c] P. E. Leite, [c] G. Perez, [g] S. M. Oliveira, [g] J. R. Araujo, [g] B. S. Archanjo, [g] M. E. Rodrigues, [h] M. Henriques, [h] J.-P. Celis, [i] T. Shokuhfar, [jk] R. Borojevic, [bl] J. M. Granjeiro [bcm] and L. A. Rocha *[abn]

The lack of osseointegration and implant-related infections are two major complications leading to failure of dental and orthopedic implants. Therefore, the development of effective titanium (Ti) implant surfaces able to display enhanced osteogenic activity and antimicrobial properties is required. In particular, titanium dioxide (TiO_2) nanotubes (NTs) have demonstrated promising features to modulate biological responses, as they may be easily tailored to achieve multiple functions. This work aims to study the ability of bio-functionalized TiO_2 NTs to induce osseointegration, and concomitantly, to avoid infection. TiO_2 NTs were bio-functionalized with calcium (Ca), phosphorous (P) and zinc (Zn), by reverse polarization anodization. Morphological and topographical features of NTs were observed through scanning electron microscopy (SEM), while surface chemistry was investigated by X-ray photoelectron spectroscopy (XPS). Biocompatibility studies were conducted with MG-63 and human mesenchymal stem cells (hMSCs) through MTT assay. Furthermore, cell morphology and cytoskeleton organization were observed by SEM and laser scanning confocal microscopy (LSCM). The osteoblastic differentiation capacity of hMSCs was studied by real-time PCR, as well as their angiogenesis ability by measuring the total release of vascular endothelial growth factor (VEGF). Finally, viability of *Staphylococcus aureus* (*S. aureus*) was assessed by live/dead bacterial viability assay. Results show that bio-functionalized TiO_2 nanotubular surfaces are biocompatible and modulated cell morphology. In particular, NTs enriched with Ca, P, and Zn, induced to significantly up-regulated levels of bone morphogenetic protein 2 (BMP-2) and osteopontin (OPN) genes of hMSCs, when compared to conventional NTs. TiO_2 nanotubular surfaces induced hMSCs to release a higher amount of VEGF, and significantly reduced the bacterial viability, both when compared to adequate Ti controls. In conclusion, the superimposition of TiO_2 nanotubular-textured surfaces and their enrichment with Ca, P, and Zn, is a very promising approach for the development of novel bio-selective implant surfaces able to improve osseointegration and avoid infection.

Received 26th July 2017
Accepted 11th October 2017

DOI: 10.1039/c7ra08263k

rsc.li/rsc-advances

Open Access Article. Published on 25 October 2017. Downloaded on 28/10/2017 17:10:08.
This article is licensed under a Creative Commons Attribution 3.0 Unported Licence.

[a]*CMEMS – Center of MicroElectroMechanical Systems, Department of Mechanical Engineering, University of Minho, Azurém, 4800-058 Guimarães, Portugal. E-mail: sofiafonso@msn.com*

[b]*IBTN/BR – Brazilian Branch of the Institute of Biomaterials, Tribocorrosion and Nanomedicine, Faculty of Sciences, UNESP – Universidade Estadual Paulista, 17033-360 Bauru, SP, Brazil. E-mail: lrocha@fc.unesp.br*

[c]*Directory of Life Sciences Applied Metrology, National Institute of Metrology, Quality and Technology, 25250-020 Duque de Caxias, RJ, Brazil*

[d]*Postgraduate Program in Translational Biomedicine, University of Grande Rio – UNIGRANRIO, 25070-000 Duque de Caxias, RJ, Brazil*

[e]*Postgraduate Program in Biotechnology, National Institute of Metrology, Quality and Technology, 25250-020 Duque de Caxias, RJ, Brazil*

[f]*Brazilian Center for Research in Physics, 22290-180 Rio de Janeiro, RJ, Brazil*

[g]*Materials Metrology Division, National Institute of Metrology Quality and Technology, 25250-020 Duque de Caxias, RJ, Brazil*

[h]*CEB – Centre of Biological Engineering, University of Minho, Campus de Gualtar, 4710-057 Braga, Portugal*

[i]*Department of Materials Engineering, KU Leuven, 3001 Leuven, Belgium*

[j]*Department of Bioengineering, University of Illinois at Chicago, 60607 Chicago, IL, USA*

[k]*IBTN/US – American Branch of the Institute of Biomaterials, Tribocorrosion and Nanomedicine, University of Illinois at Chicago, 60612 Chicago, IL, USA*

[l]*Center of Regenerative Medicine, Faculty of Medicine of Petrópolis – FASE, 25680-120 Petrópolis, RJ, Brazil*

[m]*School of Dentistry, Fluminense Federal University, 24220-900 Niterói, RJ, Brazil*

[n]*Faculdade de Ciências, Departamento de Física, Universidade Estadual Paulista – UNESP, 17033-360 Bauru, SP, Brazil*

This journal is © The Royal Society of Chemistry 2017

Open Access Article. Published on 25 October 2017. Downloaded on 28/10/2017 17:10:08.
This article is licensed under a Creative Commons Attribution 3.0 Unported Licence.

1. Introduction

Titanium (Ti) and its alloys are the most commonly used materials for orthopedic and dental implants applications owing their excellent mechanical properties, corrosion resistance and biocompatibility.[1,2] The good corrosion resistance and biocompatibility of Ti-based materials, are associated with their ability to form a stable and tightly adherent TiO_2 thin film (1.5–10 nm in thickness) when exposed to oxygen.[1,3] Nonetheless, the lack of a functional implant–bone interface (*i.e.* poor osseointegration), extensive inflammation, and bacterial infection, have been currently reported as the main causes of failure of Ti-based implants.[4–7]

Implant-related infections are often the result of bacteria adhesion on implant surface during surgery,[4,8] with *S. aureus* accounting for 70% of orthopedic implants infections.[5] Infection may lead to extensive revision surgeries, extended antibiotic treatment, tissue integration impairment, significant health care expenses, and in some cases, even death.[8,9] Furthermore, aseptic loosening is responsible for >70% hip revision surgeries over the mid- and long-term.[10] As concerns dental implants, studies conducted for a follow up period of 8 to 10 years reported failure rates of 2–9%, mainly associated to bone loss and/or inflammation as well as implant mobility.[11,12] The number of dental implant procedures is expected to boost in the near future, not only because life expectancy is increasingly high, but also because dental implant therapies have become progressively adopted as a treatment option for replacing missing teeth.[13] Therefore, if implant-related complications are not surmounted, the number of failures is expected to rise within the upcoming years.

The demand for new and innovative strategies aiming the synthesis of efficient implant surfaces has attracted the attention of worldwide researchers, as a strategy to mitigate failures of hip and dental implants. The modification of implant surface features has been currently adopted, and improved biological responses have been achieved through the creation of rough surfaces with an enhanced chemistry and a more compatible morphology/topography for bone cells.[3,14–16] In particular, nanostructures have demonstrated to play a fundamental role on biological responses, by mimicking the nanoscale features of bone.[3,17,18] Anodization is a simple, versatile, and low-cost technique that has been widely used to fabricate TiO_2 NTs in Ti surfaces, as the next generation of dental and orthopedic implants. TiO_2 nanotubular surfaces have become increasingly recognized to enhance osteoblasts and mesenchymal stem cells (MSCs) functions, *e.g.* adhesion, proliferation, and differentiation,[19–22] or even to reduce inflammation and impair bacterial adhesion or survival.[23–26]

Functionalization attempts of TiO_2 NTs have been widely reported by immersion, electrochemical deposition, plasma spraying, sputtering, and sol–gel processes.[27–30] Beyond the promising potential to induce osseointegration and reduce infection, nanotubular surfaces can behave as effective drug delivery systems. A successful example of a drug delivery system based on TiO_2 NTs was reported by Hu *et al.* (2012)[31] The authors loaded TiO_2 NTs with BMP-2 and covered them with multilayered coatings of gelatin/chitosan for controlled drug release. The system demonstrated ability to promote osteoblastic differentiation of MSCs. For tailoring TiO_2 NTs with advanced functionalities, various attempts have been performed through the incorporation of a wide variety of bioactive and/or antimicrobial agents into their cavities, such as modular peptides, anti-inflammatory and/or anti-infectious drugs, as well as inorganic bioactive elements such as silver (Ag), Zn, P, and Ca.[2,27,31–38] In particular, Zn appears as a very interesting regulator of bone formation, since Zn^{2+} ions can regulate various intracellular signaling cascades involved in osteoblastic differentiation.[39] Previous studies have demonstrated that Zn promotes the expression of bone-related genes, as well as stimulate osteoblast proliferation and mineralization.[33,40] Huo *et al.* (2013)[33] produced TiO_2 NTs incorporated with Zn by hydrothermal treatment, and the amount of Zn could be adjusted by varying nanotube diameter and length. The authors concluded that the inclusion of Zn provided relevant intrinsic antibacterial properties against *S. aureus*, as well as an excellent osteogenesis inducing ability, as shown by higher alkaline phosphatase (ALP) synthesis and mineralized nodules formation by bone MSCs. The beneficial effect of Zn was also shown by Yusa *et al.* (2016)[41] after incorporation of this element on Ti surfaces. As a result of this, human dental pulp stem cells presented significantly up-regulation levels of osteoblast-related genes of runt-related transcription factor-2 (RUNX-2), collagen type-1 (COL-1), BMP-2, ALP, OPN, and VEGF.

The next generation of orthopedic and dental implants displaying both osteogenic and antibacterial properties is required to achieve improved clinical performances. In a recent work of our group,[32] a novel and promising strategy for functionalization of TiO_2 NTs was reported, by incorporation of Ca and P *via* reverse polarization anodization processes. Bio-functionalized TiO_2 NTs displayed the ability to improve cell functions and minimize biodegradation of Ti and conventional NTs by corrosion. To understand the bio-functionalization mechanisms of conventional TiO_2 NTs by reverse polarization anodization, an additional in-depth study was recently published by our group.[42] One of its main outcomes relies on the formation of an interfacial nanothick oxide film as a consequence of anodization of TiO_2 NTs in Ca/P and Ca/P/Zn-based electrolytes. Furthermore, in an additional study, we discovered that the tribocorrosion behavior of bio-functionalized TiO_2 NTs was significantly improved compared to conventional TiO_2 NTs, in artificial saliva.[43] The higher electrochemical stability and lower mechanical degradation of the films were found correlated with their improved adhesion strength to the Ti substrate, granted by the formation of the interfacial film during bio-functionalization treatments. Therefore, besides biocompatible, bio-functionalized TiO_2 NTs display superior resistance to withstand corrosive and tribocorrosive actions, as compared to pure Ti and conventional TiO_2 NTs. These are very promising candidates to minimize implant degradation *in vivo*, and subsequently contribute for the establishment of a stable bone-implant anchorage, enhancing the implant life span. However, in-depth biological studies are still

Open Access Article. Published on 25 October 2017. Downloaded on 28/10/2017 17:10:08.
This article is licensed under a Creative Commons Attribution 3.0 Unported Licence.

missing to assess the clinical feasibility of the multifunctional nanotubular systems for osseointegrated implants applications.

In the present work, the incorporation of Ca, P and Zn into TiO_2 NTs was achieved through the previously reported methodology, and the influence of bio-functionalized nanotubular surface features on osteoblast-like and MSCs functions was studied. Beyond cell viability and adhesion ability, the aim was to study the differentiation of MSCs through the expression of osteoblast-related genes (RUNX-2, ALP, COL-1, BMP-2 and OPN) and VEGF synthesis, and furthermore, the impact of bio-functionalization on the adhesion and viability of *S. aureus*. This study brings novel and important insights on the influence of the morphological, topographical and physicochemical properties of bio-functionalized TiO_2 NTs to enhance the adhesion, differentiation, as well as the release of VEGF by hMSCs, and simultaneously, to decrease bacterial viability.

2. Materials and methods

2.1. Synthesis and characterization of bio-functionalized TiO_2 NTs

Pure titanium (Ti, 99.7%) foils (thickness 0.25 mm) were purchased (Sigma-Aldrich, St. Louis, MO, USA) and cut into 10 mm × 10 mm squares. These samples were chemically etched in a solution containing 10 vol% nitric acid (HNO_3) and 2 vol% hydrofluoric acid (HF) for 10 min. Cleaning of both groups of samples was performed in the ultrasonic bath in isopropanol (10 min) followed by distilled water (5 min), and finally dried at room temperature. Cleaned Ti samples were termed as TiP and TiE before and after chemical etching, respectively.

After chemical etching and cleaning, TiE samples were connected to an electrochemical cell with a two-electrode configuration and connected to a dc power supply (KEYSIGHT, N5751A) set with a limiting current of 2.5 A. A graphite rod was used as the cathode and TiE samples as the anode. TiO_2 NTs were synthesized by two-step anodization of TiE samples in an optimized electrolyte constituted of ethylene glycol (EG, Sigma-Aldrich, St. Louis, MO, USA), 0.3 wt% ammonium fluoride (NH_4F, ammonium fluoride, Sigma-Aldrich, St. Louis, MO, USA) and 3 vol% distilled water, as reported in our previous study.[32] Firstly, TiE samples were anodized at 60 V for 1 h under magnetic stirring (150 rpm) followed by ultrasonic cleaning in isopropanol (15 min) and distilled water (5 min). Secondly, the resulting nanopatterned surfaces were anodized for 30 min at the previous conditions for nanotube growth. Finally, the anodized samples were cleaned in isopropanol (10 min), distilled water (5 min) and dried at room temperature. The resulting TiO_2 nanotubular samples were named as NT.

Afterwards, the bio-functionalization treatments of NT samples were performed following a novel methodology described in our previous work,[32] which relies on reverse polarization and anodization treatments of TiO_2 NTs. In brief, the electrochemical treatments were conducted in an aqueous electrolyte composed of 0.35 M calcium acetate (calcium acetate monohydrate, Sigma-Aldrich, St. Louis, MO, USA) and 0.04 M β-glycerolphosphate (β-GP) (β-glycerolphosphate disodium salt pentahydrate, Sigma-Aldrich, St. Louis, MO, USA), as the source of Ca and P respectively.

The cathodic and anodic treatments were conducted by using the previously mentioned dc power supply. For reverse polarization step, the NT samples were set as the cathode and the graphite rod as the anode, and both were immersed in the Ca/P-based electrolyte 2 cm distanced. The surfaces were reverse polarized for 30 s, followed by anodization in the same electrolyte for 30 min at 100 V. Aiming the incorporation of Zn, 0.35 M zinc acetate (zinc acetate dihydrate, Sigma-Aldrich, St. Louis, MO, USA) was added to the previous Ca/P-based electrolyte and bio-functionalization treatments of NT samples were conducted at the previous conditions. The reverse polarization and anodization processes were conducted at room temperature (22 to 24 °C) and under magnetic stirring (200 rpm). Finally, the samples were cleaned in isopropanol (10 min), distilled water (5 min) and dried at room temperature. The resulting TiO_2 NTs enriched with Ca and P were named as NT-Ca/P, while the ones containing Ca, P and Zn were named as NT-Ca/P/Zn.

The surface morphology and chemical composition of all the samples were analyzed by Scanning Electron Microscopy (SEM, FEI Nova NanoLab 600) and Energy Dispersive X-ray Spectroscopy (EDS). EDS spectra were collected using 15 kV accelerating voltage with the samples 50° tilted, to guarantee the acquisition of more signal from TiO_2 NTs and less from Ti substrate. Chemical composition of the surfaces was further investigated by X-ray Photoelectron Spectroscopy (XPS, Escaplus system, Omicron Nanotechnology) using Mg Kα as the X-ray source at 1253.6 eV. Sputter-etch cleaning of samples was carried out operated at 1 kV and 5 mA for 20 min. High resolution spectra were acquired with a resolution of 0.08 eV at a pass energy of 40 eV. Binding energy of C 1s peak at 284.6 eV was used as the reference binding energy for calibration.

2.2. Biological characterization

Prior to cell culture experiments, the surfaces (including their backsides) were sterilized by 2 h immersion in ethanol 70% (v/v) followed by 2 h of ultraviolet light irradiation, in a sterile culture hood.

2.2.1. Culture of human osteosarcoma MG-63 cells. Human osteosarcoma MG-63 cells (ATCC number CRL-1427™) were provided by Rio de Janeiro cell bank and were used for cell–materials interactions studies. Osteosarcoma cells (osteoblast-like cells) are derived from malignant bone tumors and are commonly used for osteoblastic models.[44] Osteoblast-like MG-63 cells in passage 105 were cultured in standard culture plates in Dulbecco's High Glucose Modified Eagles Medium (DMEM High Glucose, Lonza) supplemented with 10% (v/v) of fetal bovine serum (FBS, Vitrocell, Embriofile) and 1% (v/v) of penicillin–streptomycin (Sigma-Aldrich) in a humidified atmosphere with 5% carbon dioxide (CO_2) at 37 °C. The culture medium was changed every three days. For cell culture experiments, at approximately 80% confluence, the adherent cells were washed with phosphate buffered solution (PBS) and enzymatically detached with trypsin.

Open Access Article. Published on 25 October 2017. Downloaded on 28/10/2017 17:10:08.
This article is licensed under a Creative Commons Attribution 3.0 Unported Licence.

2.2.2. Culture of primary human mesenchymal stem cells. Although cells derived from osteosarcoma are regularly used as osteoblastic models, these are derived from malignant bone tumors consisting of cells with abnormal functionalities in regards to the gene expression profiles and extracellular proteins translation, as compared to normal osteoblasts.[44] Therefore, to better predict the influence of surface features on human healthy cells, studies were also performed with primary human mesenchymal stem cells (hMSCs). These cells are known to play a major role in bone formation and regeneration,[45] therefore these studies become fundamental to strengthen our findings and predict real *in vivo* responses. In this study, hMSCs were isolated from bone marrow after surgical procedures on two adult healthy donors. The consent was obtained from all the individuals and all the procedures were approved by the ethics committee of Arthur Sá Earp Neto Faculty and Faculty of Medicine of Petrópolis (CAAE number: 46618615.8.0000.5245). The cells were negative for mycoplasma[46] and authenticated by STR analysis.[47]

Briefly, to isolate the cellular fraction, the collected bone marrow was homogenized in a vortex for three cycles of 15 s. Afterwards, it was washed in PBS and homogenized again followed by centrifugation for 15 min. After this step, the supernatant was discarded and the pellet was resuspended in Iscove's medium (Sigma-Aldrich) supplemented as follows: 20% (v/v) FBS; 1% (v/v) ciprofloxacin antibiotic (Isofarma); 10% (v/v) essential amino acids; 10% (v/v) pyruvate; 10% (v/v) glutamine; and 10% (v/v) vitamins. After determination of cell concentration, the cellular suspension was cultured in sterile cell culture flasks (1×10^7 cells/25 cm^2) with fresh supplemented Iscove's medium, and placed in the incubator at 37 °C and 5% CO_2. After 24 h post-seeding, the culture medium was replaced for the first time, and then it was changed every two – three days. *In vitro* experiments were carried out with hMSCs at 2–3 passages. At approximately 80% confluence, the adherent cells were washed with PBS and enzymatically detached with trypsin.

For osteoblastic differentiation, hMSCs were cultured with Iscove's medium supplemented with 10 mM β-Glycerolphosphate (Sigma-Aldrich), 50 μg mL^{-1} ascorbic acid-2 phosphate (Sigma-Aldrich) and 100 nM dexamethasone (Sigma-Aldrich). This supplement is currently used to stimulate the differentiation of MSCs into osteoblasts.[45] Throughout this work, Iscove's osteogenic medium was named as Iscove's OM.

2.2.3. Cell viability. The viability of MG-63 cells and hMSCs cultured on TiP, TiE, NT, NT-Ca/P and NT-Ca/P/Zn samples was investigated through MTT (3-(4,5-dimethyl-2-thiazolyl)-2,5-diphenyl-2*H*-tetrazolium bromide) reduction assay. Firstly, the samples were placed (in triplicate per test condition) in 24-well polystyrene culture places, and afterwards 2×10^4 cells were seeded on each sample. The cells were additionally cultured on the wells of the culture plate for cell viability control. After seeding, the cells were incubated at 37 °C in a 5% CO_2 atmosphere and the culture medium was changed every two – three days. MG-63 cells and hMSCs were cultured with DMEM High Glucose and OM Iscove's culture medium, respectively. Each culture medium was supplemented as previously described.

Cell viability was evaluated after one and six days of culture. After each culture period, the cells were incubated with MTT (0.5 mg mL^{-1}, Sigma-Aldrich, MO, USA) for 4 hours at 37 °C. The MTT assay allows the assessment of metabolically active viable cells, which convert MTT into a purple colored formazan product.[48] After the incubation period the formazan was solubilized by dimethyl sulfoxide (DMSO) and the absorbance was measured at $\lambda = 570$ nm and $\lambda = 690$ nm (background) on a microplate reader spectrometer (Infinite® 200 PRO, Tecan).

Three independent experiments were carried out for cell viability studies with MG-63 and hMSCs, and only hMSCs derived from one patient were used to conduct these tests.

2.2.4. Cell morphology, spreading and adhesion. Osteoblast-like MG-63 cells and hMSCs were seeded on TiP, TiE, NT, NT-Ca/P and NT-Ca/P/Zn samples for 24 h. The studies with hMSCs were carried out only with cells extracted from one single patient. For this purpose, 1×10^4 cells were seeded on materials surfaces, which had been previously placed into 24-well culture plates. MG-63 cells were cultured as described above. After one day of incubation, the cells were washed in PBS and fixed for 2 h (room temperature) with 2.5% (v/v) glutaraldehyde (Electron Microscopy Sciences) in 0.1 M cacodylate buffer, pH 7.4 (Electron Microscopy Sciences). Afterwards, the samples were washed three times (5 min each) in cacodylate buffer and then postfixed with 1% (v/v) osmium tetroxide in distilled water for 1 h, in dark conditions. After washing steps in cacodylate buffer and distilled water, the cells were dehydrated in series of graded ethanol solutions of 15%, 30%, 50%, 70%, 90% and 100% (v/v), followed by critical point drying (Leica EM CPD030, Leica microsystems, Austria). Finally, the samples were placed onto a stub and sputter coated with carbon. The cell morphology was then observed in a FEI Magellan 400 microscope.

Morphological features of hMSCs were also investigated by laser scanning confocal microscopy by cytoskeleton staining of actin filaments and nucleus. Briefly, 1×10^4 hMSCs were seeded on materials surfaces for 2 h incubation period in Iscove's medium. After this time, the cells were washed in PBS and fixed with a solution of 4% (v/v) paraformaldehyde in PBS for 20 min. Afterwards, hMSCs were washed twice in PBS (5 min each) and permeabilized with 0.1% (v/v) Triton X-100 in PBS, for 30 minutes. After washing in PBS the cells, were incubated in 50 nM NH_4Cl in PBS for 15 min for blocking of non-specific binding sites. Then, hMSCs were incubated with Alexa Fluor® 546 Phalloidin (Molecular Probes, Life Technologies) in darkness for 60 min, and after washing twice in PBS (5 min each), the nucleus was stained with 4′,6-diamidino-2-phenylindole, dehydrochloride (DAPI) (Molecular Probes, Life Technologies) for 10 min. At the end, the cells were imaged using a Leica TCS SP3 confocal microscope.

2.2.5. Expression of osteoblast-related genes. The expression levels of osteoblast-related genes were determined by real-time quantitative polymerase chain reaction (qPCR). hMSCs were seeded (2×10^4 cells) on TiP, TiE, NT, NT-Ca/P and NT-Ca/P/Zn samples and incubated for 14 days in OM Iscove's. Four different samples were used per each condition. After 14 days of incubation, the cells were washed in PBS and the total RNA was extracted using RNeasy Plus mini kit (Qiagen) in accordance

Open Access Article. Published on 25 October 2017. Downloaded on 28/10/2017 17:10:08.
This article is licensed under a Creative Commons Attribution 3.0 Unported Licence.

with manufacturer's instructions. Afterwards, the RNA concentrations were determined by using a NanoDrop 2000c spectrophotometer (Thermo Scientific) at 260 nm (A_{260}). Only samples with A_{260}/A_{280} and A_{260}/A_{230} ratio equal or greater than 1.8 were used for the subsequent steps, since this is an indicator of absence of contamination by protein and organic compounds. After RNA extraction and quantification, first-strand cDNA was synthesized from 200 ng of RNA using SuperScript® IV First-Strand synthesis kit (Invitrogen™, Life Technologies), by following manufacturer's instructions. The qPCR experiments were carried out with a 7500 Real-Time PCR system (Applied Biosystems®) using Power SYBR® green PCR master mix (Applied Biosystems™, Life Technologies).

The relative expression of genes related to osteoblastic differentiation was determined, namely runt-related transcription factor-2 (RUNX-2), alkaline phosphatase (ALP), collagen type-1 (COL-1), bone morphogenetic protein-2 (BMP-2) and osteopontin (OPN). Their main functionalities may be summarized as follows: RUNX-2 is an essential transcription factor involved in the very early stage of osteoblast differentiation; ALP is a specific protein that displays a crucial role in osteoblast differentiation and mineralization of bone matrix; COL-1 is a key structural protein of bone matrix; BMP-2 is a protein that stimulates bone formation; and OPN is a major structural protein of bone matrix.[49–53] The nucleotide sequences of forward (F) and reverse (R) primers used for qPCR are shown in Table 1. The relative gene expression levels were determined based on the comparative Ct method (also known as $2^{-\Delta\Delta Ct}$),[54] and these were normalized to that of the endogenous housekeeping gene cancer susceptibility candidate 3 (CASC-3). Fold change values were determined with TiP as the reference group.

The qPCR assays were performed only for hMSCs and two independent experiments were carried out with cells obtained from each donor. Therefore, a total number of four independent tests ($n = 4$) were carried out.

2.2.6. Alkaline phosphatase activity and matrix mineralization. In this study, human fibroblasts (hFb) and human Saos-2 osteosarcoma cells were cultured on polystyrene culture plate wells as negative and positive controls of osteoblastic differentiation of hMSCs, respectively. Human fibroblasts were obtained from surgical procedures of a healthy donor child in accordance with a local Ethical Committee (University of Grande Rio – UNIGRANRIO, CAAE number: 46799215.1.3001.5282) and Saos-2 cells were provided by Rio de Janeiro cell bank. Saos-2 cells were used as positive control instead of MG-63 cells, because they reveal the most mature osteoblastic labelling profile.[44] Alkaline phosphatase (ALP) activity and matrix mineralization were assessed for hFb, Saos-2, and hMSCs seeded on culture plate wells (2×10^4 cells, in triplicate) for 14 and 21 days, respectively. It is noteworthy that hFb were cultured in Iscove's medium, Saos-2 in DMEM High Glucose medium, and hMSCs in Iscove's OM. DMEM high glucose and Iscove's culture media were supplemented as above described.

After 14 days of culture, the cells were washed in PBS and fixed with a solution of 4% (v/v) paraformaldehyde in PBS for 20 min. After washing in PBS, the ALP activity was detected by incubation in a mixture of naphthol AS-MX phosphate alkaline solution with fast red violet B salt (Leukocyte Alkaline Phosphatase Kit, Sigma-Aldrich), in accordance with manufacturer's instructions. Finally, images were acquired in an inverted microscope (Zeiss, Axio Observer.D1, Germany) by using a 10× objective. The matrix mineralization of cells was evaluated by Alizarin Red S staining (Sigma-Aldrich). Briefly, after culturing for 21 days, all the cells were washed in PBS and fixed with a solution of 4% (v/v) paraformaldehyde in PBS for 20 min, and then washed with distilled water. Afterwards, the cells were incubated with Alizarin red S solution 1% (wt/vol) for 30 min. Finally, the samples were washed 5× with distilled water to remove the unabsorbed dye, and images were obtained in the previous mentioned inverted microscope (10× objective).

2.2.7. Analysis of VEGF secretion. hMSCs were seeded (2×10^4 cells) on TiP, TiE, NT, NT-Ca/P and NT-Ca/P/Zn samples and incubated for 14 days in Iscove's OM. The culture medium was changed every two days. At day 14, 1 mL of the culture medium was collected with 48 h of incubation, for detection and quantification of vascular endothelial growth factor (VEGF) produced by hMSCs in contact with the different materials. VEGF detection was performed through bead-based immunoassay with the XMap Technology (Luminex Corp, USA) by using a singleplex kit (Biorad, USA). Afterwards, washes were performed using the automated washer Bio-Plex Pro (Biorad, USA). Identification and quantification of the magnetic beads containing VEGF were performed with a Bio-Plex MAGPIX system (Biorad, USA) following manufacturer's protocol. Finally, the concentration of VEGF was quantified with xPONENT software version 4.2 (Biorad, USA). These experiments were carried out in triplicate, to guarantee the repeatability of the results.

2.3. Antibacterial test

The antibacterial ability of TiO_2 nanotubular surfaces was accessed using *S. aureus* as the target organism. *S. aureus* ATCC 6538 obtained from stock solid cultures were grown in Tryptic

Table 1 Forward (F) and reverse (R) sequences of primers used for qPCR

Gene	Forward primer sequence (5′–3′)	Reverse primer sequence (5′–3′)
RUNX-2	TGGTTACTGTCATGGCGGGTA	TCTCAGATCGTTGAACCTTGCTA
ALP	ACTGGTACTCAGACAACGAGA	ACGTCAATGTCCCTGATGTTATG
COL-1	GAGGGCCAAGACGAAGACATC	CAGATCACGTCATCGCACAAC
BMP-2	ACTACCAGAAACGAGTGGGAA	GCATCTGTTCTCGGAAAACCT
OPN	AGACCTGACATCCAGTACCCT	GTGGGTTTCAGCACTCTGGT
CASC-3	AGCCTTCTTTCCTGCAACCA	GGTCCTGCTCCCATGTGTATATG

 This journal is © The Royal Society of Chemistry 2017

Open Access Article. Published on 25 October 2017. Downloaded on 28/10/2017 17:10:08.
This article is licensed under a Creative Commons Attribution 3.0 Unported Licence.

Soy Broth medium (TSB, Liofilchem) at 37 °C for approximately 24 h. Before bacterial seeding, the samples were placed inside a 24-well culture plate and all the samples were sterilized by immersion in ethanol 70% (v/v) for 2 h inside a sterile culture hood.

Bacterial concentration was determined by measuring absorbance at 620 nm (EZ Read 800 Plus Microplate reader, Biochrom), and the cell suspension was adjusted to an optical density corresponding to the final concentration of 1×10^5 cell per mL.

Samples previously sterilized by immersion in ethanol 70% (v/v) for 2 h in 24-well plates, were seeded with 1 mL of the prepared cell suspension and incubated for 2 h at 37 °C and 120 rpm. Samples were then washed twice in PBS and the viability of adherent bacteria was accessed by LIVE/DEAD® BacLight™ bacterial viability kit (Molecular Probes, Life Technologies) in accordance with manufacturer's instructions. Finally, the total number of live and dead bacteria adhered on materials surfaces was determined by fluorescence microscope (Olympus BX51, Perafita, Portugal), using a combination of the 470 to 490 nm and 530 to 550 nm optical excitation filters. A total number of 35 images were acquired for each sample, from which the number of live and dead bacteria were counted. For each testing condition, three samples were used and three independent experiments were carried out.

2.4. Statistical analysis

All the quantitative data were expressed as means ± standard deviations. The statistical tool SigmaStat 3.5 (Systat Software, San Jose, CA, USA) was used for statistical analysis with $p < 0.05$ considered as being statistically significant and $p < 0.01$ considered highly significant.

One-way ANOVA was applied to determine the differences between the different groups of surfaces and Tukey HSD post hoc analysis was used for pair-wise comparisons between groups. In particular, the statistical significance in the relative gene expression of hMSCs, measured between the control group and all the others testing groups, was determine by *t*-student test.

3. Results

3.1. Surface characterization

In this study, smooth and micron/nano-roughened Ti surfaces (TiP and TiE) were taken as control groups, whose morphologies are depicted in Fig. 1a and b respectively. The morphological and chemical surface features of TiO_2 nanotubular films synthesized by two-step anodization processes are depicted in Fig. 1c. A bone-inspired morphology was achieved at a nanoscale level, with NTs characterized by non-uniform diameters ranging from 50–90 nm, as reported in a previous study.[32] XPS studies were conducted to determine the surface chemical features of TiO_2 NTs, through which chemical elements such as Ti, oxygen (O) and fluorine (F) were detected. The individual XPS spectra of these elements were deconvoluted into their components aiming to study their binding states. The deconvoluted peaks are shown in the individual spectra of the elements with reference to the subpeak binding energy and the possible chemical compound assigned to it (Fig. 1c). The high resolution spectra of Ti $2p_{3/2}$ and O 1s confirm the presence of TiO_2 by the subpeaks found at 458.8 eV and 530 eV,[35,55,56] respectively. The energy difference of 5.7 eV for Ti $2p_{1/2}$ and Ti $2p_{3/2}$ confirms the presence of TiO_2.[55] Two additional contributions were found in Ti $2p_{3/2}$ spectrum, which are most likely related to the presence of Ti_2O_3 (456.9 eV) and Ti–OH (458.3 eV) compounds.[57,58] The O 1s spectrum showed an additional subpeak at 531.4 eV assigned both to the presence of Ti_2O_3 and Ti–OH[55,56,59] compounds. Adsorbed fluoride (F^-) ions on TiO_2 nanotubular surfaces were also found by the F 1s peak detected at 684.6 eV.[55] EDS analysis confirmed the presence of Ti, O, F and C (Fig. 1f – black curve). These results are in good agreement with our previous study,[32] in which XPS and EDS studies were carried out for NT surfaces.

The surface morphology of NT-Ca/P and NT-Ca/P/Zn samples is shown in Fig. 1d and e, respectively. No significant differences are observed on the morphological/topographical features of both bio-functionalized nanotubular surfaces compared to the non-treated ones (Fig. 1c). However, dissimilar chemical features were found after bio-functionalization treatments. NT-Ca/P surfaces are composed of Ca and P as shown by the individual XPS spectra of Ca 2p and P 2p in Fig. 1d. The Ca $2p_{3/2}$ subpeak detected at 347.6 eV, in agreement with the P 2p peak found at 132.9 eV, evidence the presence of $Ca_3(PO_4)_2$ compounds on TiO_2 NTs.[35] Furthermore, the energy found for Ca $2p_{3/2}$ subpeak may be also related to the presence of $CaHPO_4$ species, as confirmed by the P 2p subpeak found at 134.1 eV (Fig. 1d).[35] Moreover, additional contributions were found in Ca $2p_{3/2}$ main peak at 346.7 eV and 348.6 eV, which might be assigned to $CaCO_3$/CaO and CaF_2 (ref. 35, 60 and 61) compounds respectively. These findings are in accordance with XPS results reported in a previous work for similar NT-Ca/P surfaces.[32] The EDS spectrum obtained from NT-Ca/P samples (Fig. 1f – red curve) showed the presence of Ti, O, F, Ca, P, and a small amount of sodium (Na) from the anodization process. Once Na was not detected by XPS, it is probably located in deeper regions of TiO_2 NTs. As regards NT-Ca/P/Zn surfaces, Zn and P elements were detected by XPS, and the correspondent high resolution spectra are shown in Fig. 1e. Although the presence of Ca 2p was found insignificant on these surfaces by XPS, a small amount of Ca was detected by the EDS (Fig. 1f – blue curve), most probably because it is located deep in TiO_2 NTs. Furthermore, EDS analysis also showed the presence of Ti, O, F, Zn and P. The peak for Zn $2p_{3/2}$ was found at 1021.6 eV and assigned to ZnO compounds,[62] while P 2p was revealed at 133.6 eV and related to PO_4^{3-} groups adsorbed to TiO_2 NTs.[35] It is noteworthy to highlight that Ti 2p, O 1s and F 1s were also detected on NT-Ca/P and NT-Ca/P/Zn surfaces by XPS and assigned to the presence of TiO_2, Ti_2O_3 and Ti–OH, as well as F^- ions adsorbed to TiO_2 NTs (results not shown).

3.2. Biological characterization

3.2.1. Viability and adhesion of MG-63 and hMSCs. The viability of MG-63 cells (human osteoblast-like osteosarcoma

Open Access Article. Published on 25 October 2017. Downloaded on 28/10/2017 17:10:08.
This article is licensed under a Creative Commons Attribution 3.0 Unported Licence.

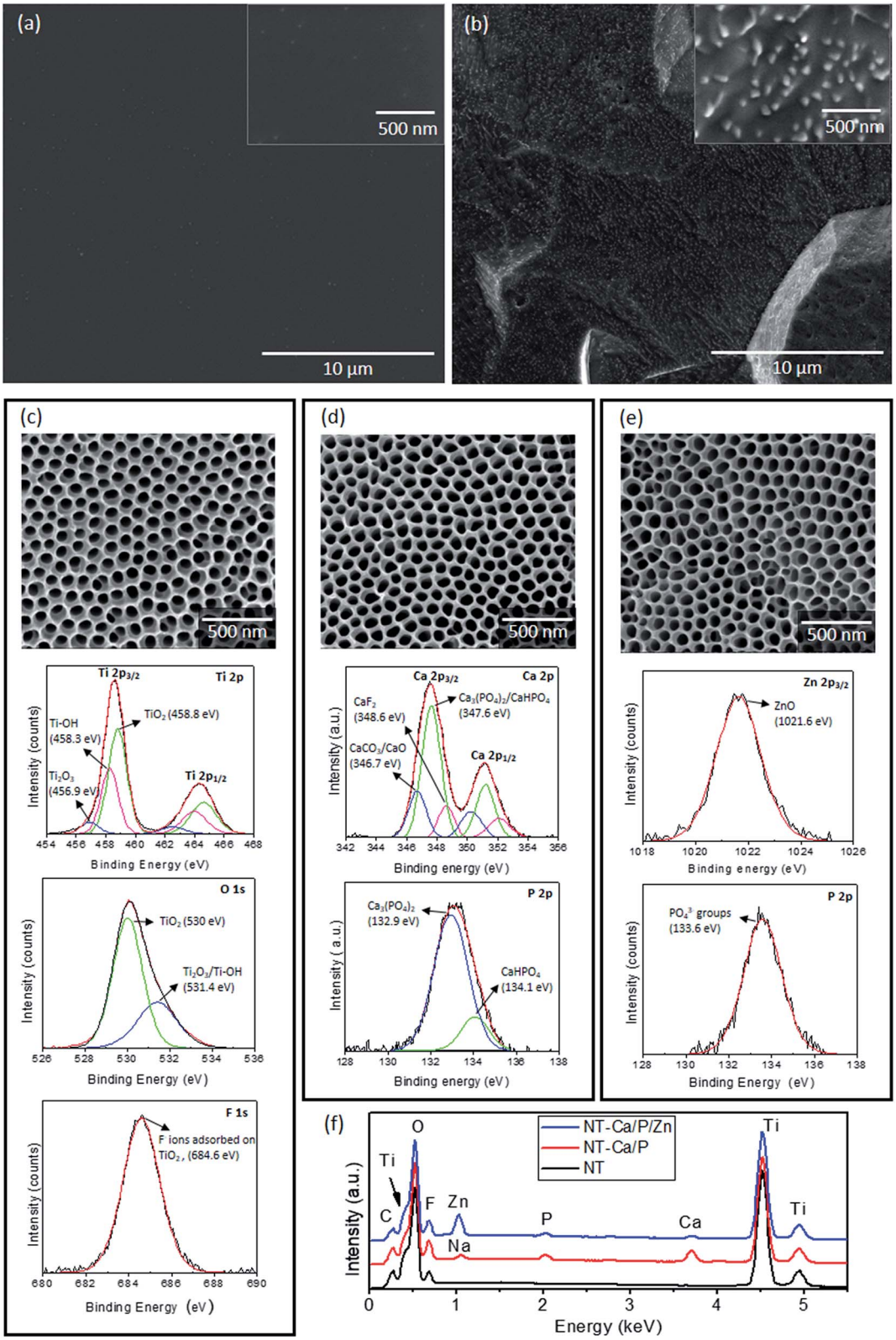


Fig. 1 SEM micrographs of (a) TiP, (b) TiE, (c) NT, (d) NT-Ca/P and (e) NT-Ca/P/Zn surfaces. The inset images in (a) and (b) intend to show the morphological/topographical surface features in more detail. The representative high resolution XPS spectra of deconvoluted Ti 2p, O 1s and F 1s detected on NT surfaces are shown in (c). Furthermore, the XPS spectra of Ca 2p and P 2p detected on NT-Ca/P surfaces are depicted in (d), while in (e) the XPS spectra for Zn $2p_{3/2}$ and P 2p detected on NT-Ca/P/Zn surfaces are shown. The information extracted from deconvolution is depicted in each individual spectrum in respect to the subpeak binding energy and possible chemical compound assigned to it. In (f) the EDS spectra acquired from NT, NT-Ca/P and NT-Ca/P/Zn samples are depicted.

This journal is © The Royal Society of Chemistry 2017

Open Access Article. Published on 25 October 2017. Downloaded on 28/10/2017 17:10:08.
This article is licensed under a Creative Commons Attribution 3.0 Unported Licence.

cell line) cultured on materials surfaces (*i.e.* TiP, TiE, NT, NT-Ca/P and NT-Ca/P/Zn) was investigated after one and six days of incubation, and the results are graphically represented in Fig. 2a. TiE surfaces were chosen also as positive control due to its well-known ability to improve osteoblast functions and by its attractiveness in clinical applications.[63] The percentage of absorbance values measured after MTT assay were converted into a percentage that was calculated in reference to TiP samples, which means that the absorbance value measured for TiP was taken as 100%. After the first day of incubation, MG-63 osteoblast-like cells adhered on TiP and on all the nanotubular surfaces displayed a significantly inferior level of metabolic activity compared to the one on TiE surfaces. After six days of culture, as expected, a significant increase of cellular metabolic activity is observed for all groups, confirming cell proliferation throughout the culture time. Interestingly, it is observed that the metabolic activity of cells adhered on TiE and all the nanotubular surfaces, was significantly superior compared to TiP surfaces. This evidences that all the groups of treated surfaces are biocompatible.

The morphology of osteoblasts adhered on the different groups of samples was investigated after 24 h of culture, and the representative SEM micrographs are shown in Fig. 2b–f. Significant differences are observed between cell morphology on Ti (Fig. 2b and c) and nanotubular surfaces (Fig. 2d–f). MG-63 cells adhered on nanotubular surfaces display a stretched and elongated shape when compared with those on Ti groups, in which they exhibit spreader morphologies apparently covering a higher surface area. In all the cases, noticeable plasma membrane protrusions (filopodia) are visible evidencing cell–surface and cell–cell interactions. Interestingly, although a high density of filopodia has been found on all the surfaces, the cytoplasmic extensions presented different features: thinner and longer on Ti-based surfaces, and thicker and shorter on nanotubular surfaces, as shown in Fig. 3a and b respectively. These differences may be observed in more detail in Fig. 3c and d. Curiously, filopodia endings display a "ball-like" morphology on Ti surfaces (Fig. 3c) compared to the flattened filopodia shape observed on nanotubular surfaces (Fig. 3d).

The biocompatibility of treated and non-treated nanotubular surfaces was also investigated for human mesenchymal stem cells (hMSCs) by MTT assay. The percentage of absorbance values are depicted in Fig. 4a after cell culture in OM for one and six days. After one day of culture, a significant lower metabolic activity was measured for cells adhered on NT-Ca/P and NT-Ca/P/Zn samples as compared to TiE, and after six days these differences were kept significant only for NT-Ca/P/Zn samples.

As regards hMSCs morphology after 24 h of adhesion, significant differences were observed for cells adhered on Ti and nanotubular samples, as previously observed for MG-63 cells. It is clearly perceived that cells adhered on nanotubular surfaces (Fig. 4d–f) present a more stretched and elongated morphology with filopodia interacting with nanotubular surfaces. On the other hand, the cells adhered on TiP and TiE

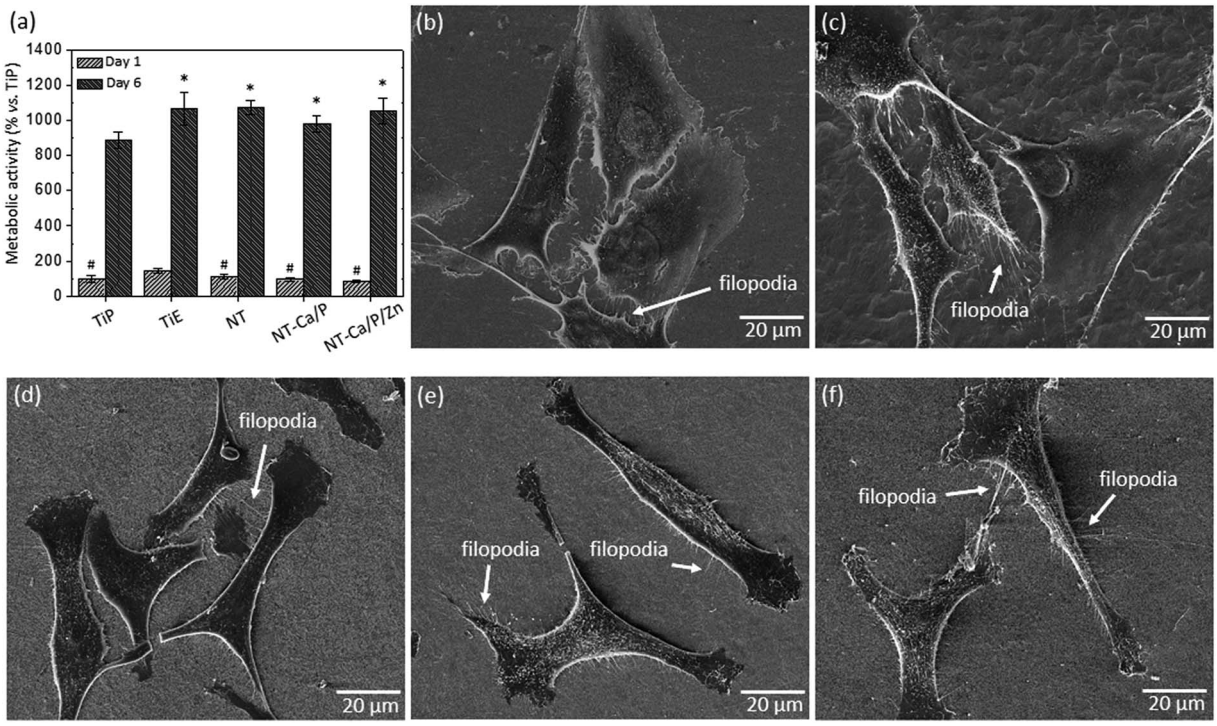


Fig. 2 (a) Metabolic activity of MG-63 cells cultured on TiP, TiE, NT, NT-Ca/P and NT-Ca/P/Zn samples after one and six days of incubation. SEM micrographs of MG-63 cells adhered on (b) TiP, (c) TiE, (d) NT, (e) NT-Ca/P and (f) NT-Ca/P/Zn samples after one day (24 h) of culture. Inset white arrows point to cytoplasmic protrusions of cells (filopodia). At day 1: (#) significantly different from TiE, $p < 0.05$; at day 6: (*) significantly different from TiP, $p < 0.05$.

Open Access Article. Published on 25 October 2017. Downloaded on 28/10/2017 17:10:08.
This article is licensed under a Creative Commons Attribution 3.0 Unported Licence.

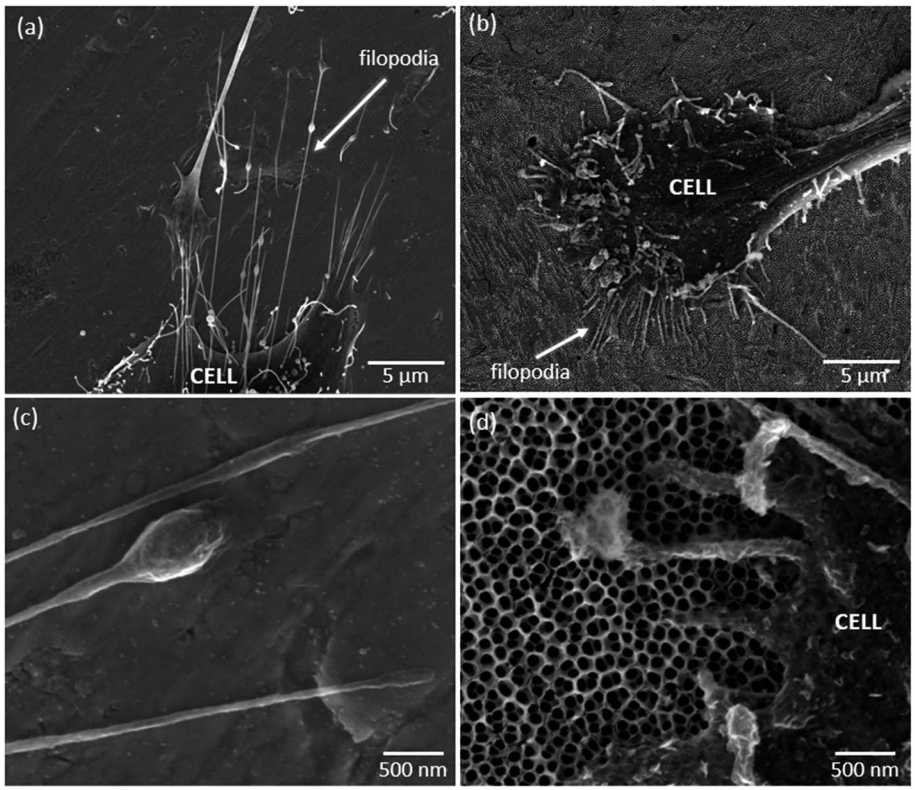


Fig. 3 SEM micrographs showing the differences between cytoplasmic protrusions (filopodia) of MG-63 cells adhered on (a) Ti and (b) nanotubular surfaces after one day (24 h) of culture. Inset white arrows point to filopodia. Higher magnified images of filopodia are shown in (c) and (d) for Ti and nanotubular surfaces, respectively.

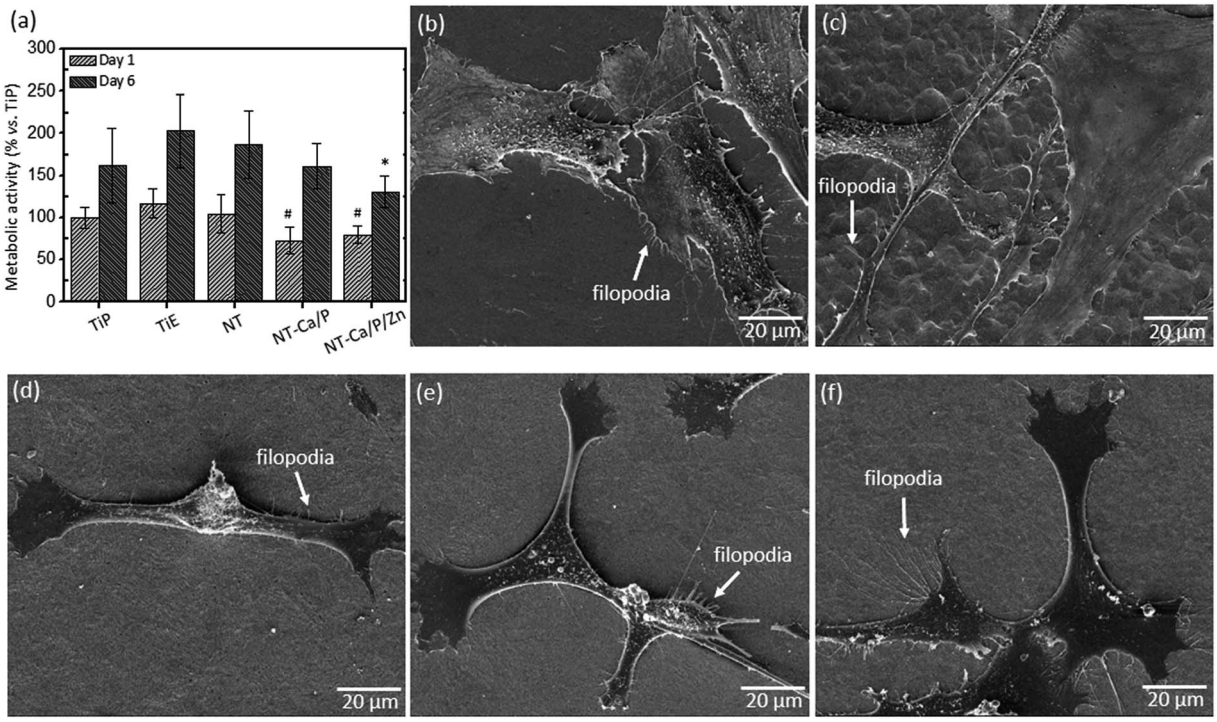


Fig. 4 (a) Metabolic activity of hMSCs cells cultured on TiP, TiE, NT, NT-Ca/P and NT-Ca/P/Zn samples after one and six days of incubation in OM. SEM micrographs of hMSCs cells adhered on (b) TiP, (c) TiE, (d) NT, (e) NT-Ca/P and (f) NT-Ca/P/Zn samples after one day (24 h) of culture. Inset white arrows point to cytoplasmic protrusions of cells (filopodia). At day 1: (#) significantly different from TiE, $p < 0.05$; at day 6: (*) significantly different from TiE, $p < 0.05$.

 This journal is © The Royal Society of Chemistry 2017

Open Access Article. Published on 25 October 2017. Downloaded on 28/10/2017 17:10:08.
This article is licensed under a Creative Commons Attribution 3.0 Unported Licence.

surfaces (Fig. 4b and c), show a less defined morphology, and are spreader along the surface apparently covering a larger surface area. Filopodia are also observed for these cells evidencing interaction with the surface and neighboring cells.

In order to understand the cytoskeleton organization of hMSCs adhered on Ti and nanotubular surfaces in an early stage of adhesion, the actin filaments were observed by confocal fluorescence microscopy and the results are shown in Fig. 5. As observed, clear differences are noticed between the morphology of hMSCs adhered on Ti (*i.e.* TiP and TiE) and nanotubular surfaces (*i.e.* NT, NT-Ca/P and NT-Ca/P/Zn). The cells on Ti surfaces present a rounder morphology compared to the cells adhered on nanotubular surfaces, and undergone a remarkably less stretching. On the other hand, the cells on nanotubular surfaces are already very well stretched and elongated. This indicates that cells settled faster on TiO_2 NTs, and that they have quickly interacted and became adapted to these surfaces earlier than on Ti. The cells on all the nanotubular surfaces present a typical morphology characterized by a stretched and tinny cell body (Fig. 5c–e). Nevertheless, the cell endings are spreader along the surfaces compared to the main body, evidencing a higher contact and an intense interaction with the substrate through a high number of filopodia (Fig. 5e) and stress fibers formation, which are key signals for cell adhesion and migration.[31]

3.2.2. Osteogenic differentiation of hMSCs. To better characterize the osteoblastic phenotype of hMSCs cultured on standard culture plates in OM, primary human fibroblasts (hFb) and osteoblast-like Saos-2 cells (Saos-2) were taken as negative and positive controls, respectively. The colorimetric assay for detection of ALP was carried out after 14 days of culture for the three groups of cells, and the results are shown in Fig. 6. As observed in Fig. 6a, hFb are not producers of ALP, contrarily to Saos-2 (Fig. 6b), as would be expected since Saos-2 cells exhibit mature osteoblast phenotype.[44] As evidenced from Fig. 6c, hMSCs cultured in OM are producers of ALP after 14 days of culture, indicating that the cells have undergone osteoblastic differentiation. This was confirmed by matrix mineralization performed after 21 days of culture for the same groups of cells, for which mineralization occurred in Saos-2 (Fig. 6e) and hMSCs (Fig. 6f), contrarily to hFb (Fig. 6d).

The relative expression of osteogenesis-related genes, namely runt-related transcription factor 2 (RUNX-2), alkaline phosphatase (ALP), collagen type-1 (COL-1), bone morphogenetic protein-2 (BMP-2) and osteopontin (OPN) was determined to investigate whether morphological/topographical and chemical features of Ti and nanotubular surfaces influence the osteogenic differentiation of hMSCs. The gene expression of the different targets is shown in Fig. 7, and the values are presented as fold changes, which were calculated in reference to the

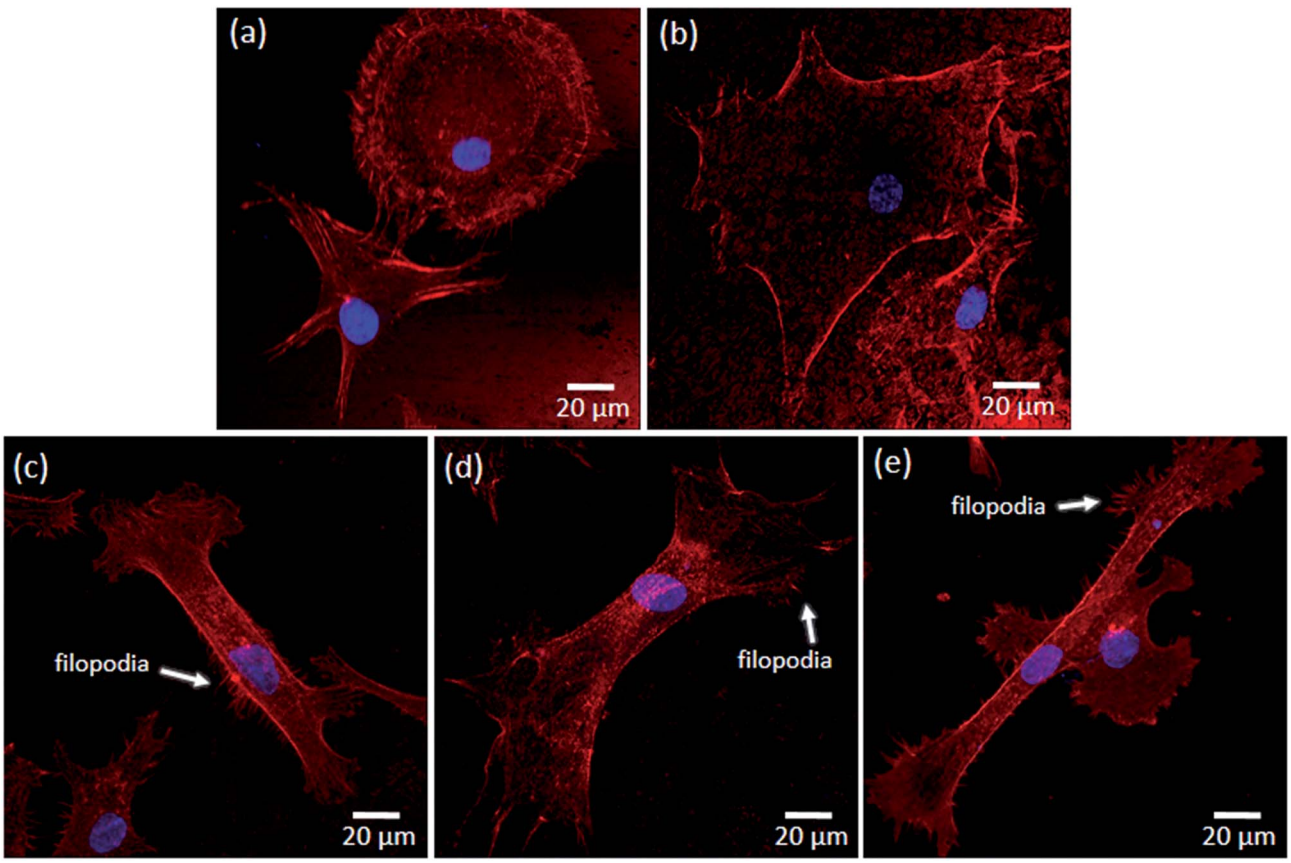


Fig. 5 Confocal fluorescence images showing actin cytoskeleton organization of hMSCs adhered on (a) TiP, (b) TiE, (c) NT, (d) NT-Ca/P, and (e) NT-Ca/P/Zn samples after 2 h of incubation.

Open Access Article. Published on 25 October 2017. Downloaded on 28/10/2017 17:10:08.
This article is licensed under a Creative Commons Attribution 3.0 Unported Licence.

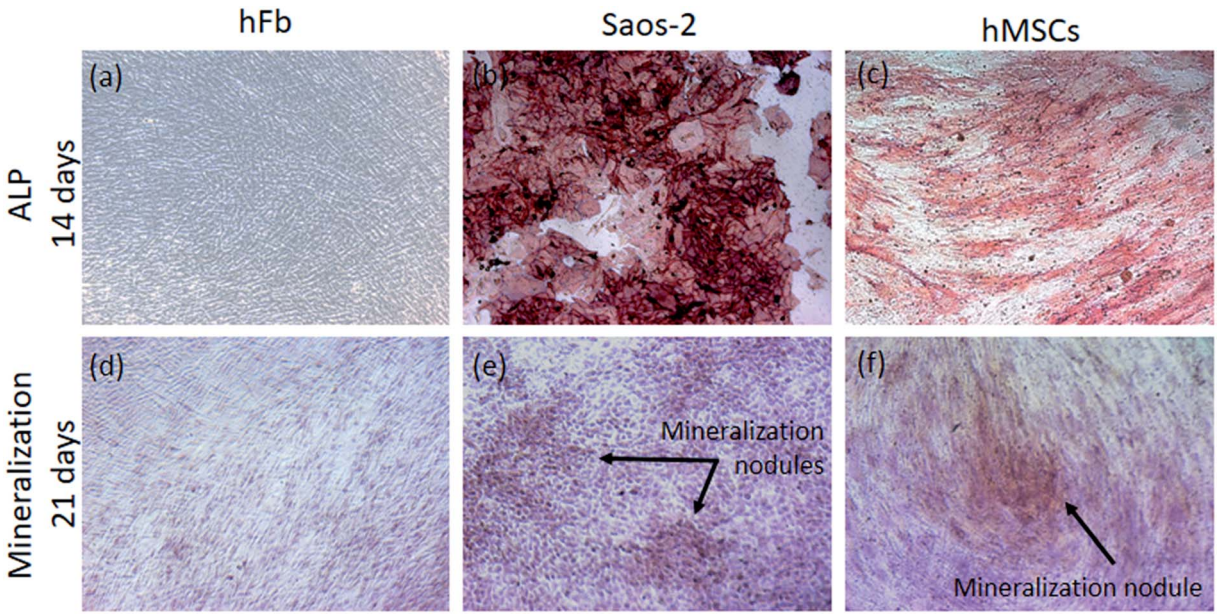


Fig. 6 Optical micrographs of (a) hFb, (b) Saos-2 and (c) hMSCs after colorimetric assay for detection of ALP (14 days of culture). The colorimetric assay for detection of mineralization nodules was also carried out and the optical micrographs of (d) hFb, (e) Saos-2 and (f) hMSCs are shown for 21 days of culture.

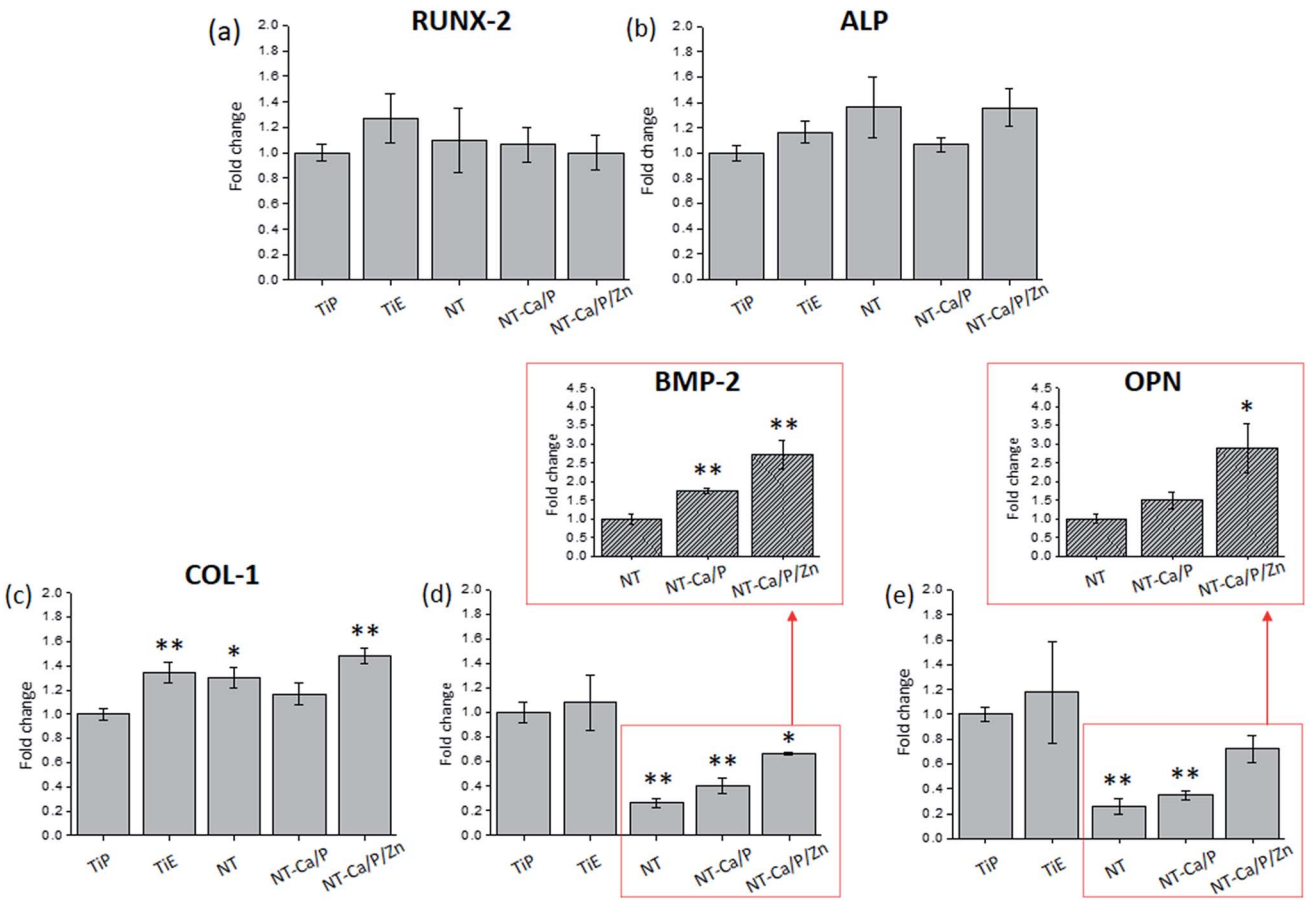


Fig. 7 Relative expression of (a) RUNX-2, (b) ALP, (c) COL-1, (d) BMP-2 and (e) OPN genes of hMSCs cultured on TiP, TiE, NT, NT-Ca/and NT-Ca/P/Zn samples after 14 days of incubation in OM. Fold change values were calculated against the control TiP. (*), significantly different from TiP, $p < 0.05$; highly significantly different from TiP (**) $p < 0.01$. The insets in (d) and (e) show the relative gene expression of BMP-2 and OPN respectively, whose values were calculated with NT samples as the control group. (*), significantly different from NT, $p < 0.05$; highly significantly different from NT (**) $p < 0.01$. Gene expression levels were normalized against housekeeping gene CASC-3.

This journal is © The Royal Society of Chemistry 2017

Open Access Article. Published on 25 October 2017. Downloaded on 28/10/2017 17:10:08.
This article is licensed under a Creative Commons Attribution 3.0 Unported Licence.

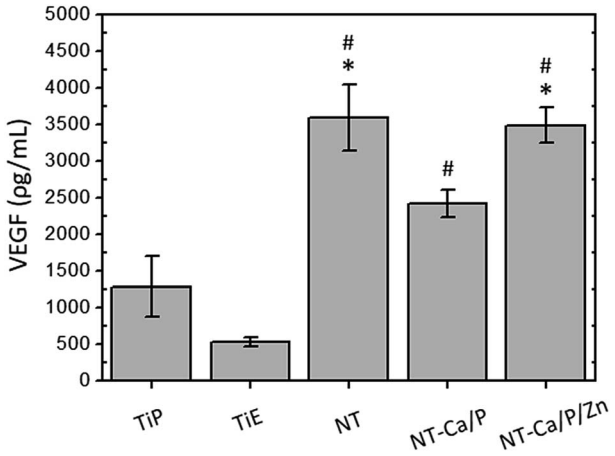


Fig. 8 Amount of VEGF produced by hMSCs adhered on TiP, TiE, NT, NT-Ca/P and NT-CA/P/Zn surfaces after 14 days of culture in OM. (*) significantly different from TiP, $p < 0.01$; (#) significantly different from TiE, $p < 0.01$.

control group TiP. The results show that while no significant differences were found for the expression of RUNX-2 (Fig. 7a) and ALP (Fig. 7b) genes within the different groups, statistically significant differences were observed for COL-1 (Fig. 7c), BMP-2 (Fig. 7d) and OPN (Fig. 7e) genes expression.

The expression of COL-1 was significantly up-regulated in hMSCs cultured on TiE ($p < 0.01$), NT ($p < 0.05$) and NT-Ca/P/Zn ($p < 0.01$) surfaces compared to the control group TiP (Fig. 7c). Instead, the relative expression of BMP-2 was found significantly down-regulated for NT ($p < 0.01$), NT-Ca/P ($p < 0.01$) and NT-Ca/P/Zn ($p < 0.05$) surfaces relatively to TiP (Fig. 7d). Moreover, OPN gene expression was also down-regulated in hMSCs present on NT ($p < 0.01$) and NT-Ca/P ($p < 0.01$) surfaces (Fig. 7e). Interestingly, a clear trend of a higher expression of both BMP-2 and OPN genes for NT-Ca/P/Zn is observed, when compared to NT-Ca/P and NT samples, as observed in Fig. 7d and e. To further confirm this trend, the relative expression of BMP-2 and OPN genes was determined settling NT as the reference group, and the results are shown in the insets graphs in Fig. 7d and e, respectively. As clearly observed, the expression of BMP-2 gene was significantly higher for NT-Ca/P ($p < 0.01$), and even more pronounced for NT-Ca/P/Zn surfaces ($p < 0.01$) compared to NT control group. Furthermore, significantly higher differences ($p < 0.05$) were also found for the relative gene expression of OPN for NT-Ca/P/Zn samples as compared to NT. The BMP-2 and OPN genes were around 3 times more expressed in hMSCs cultured on the nanotubular surfaces enriched with Zn, when compared to conventional nanotubular surfaces. It is noteworthy that significantly different ($p < 0.05$) gene expression levels of BMP-2 and OPN genes were also observed for NT-Ca/P/Zn compared to NT-Ca/P samples, with fold change values determined by taking NT-Ca/P surfaces as the reference (results not shown).

3.2.3. VEGF release by hMSCs. To investigate the possible role of surface characteristics on vascularization process, the quantity of vascular endothelial growth factor (VEGF) produced by hMSCs was quantified after 14 days of culture in OM, and the results are shown in Fig. 8. The cells in contact with NT and NT-Ca/P/Zn surfaces produced significantly higher VEGF amounts compared to the ones on TiP and TiE surfaces ($p < 0.01$). Furthermore, a significantly higher extent of VEGF was also released by cells on NT-Ca/P compared to TiE surfaces ($p < 0.01$).

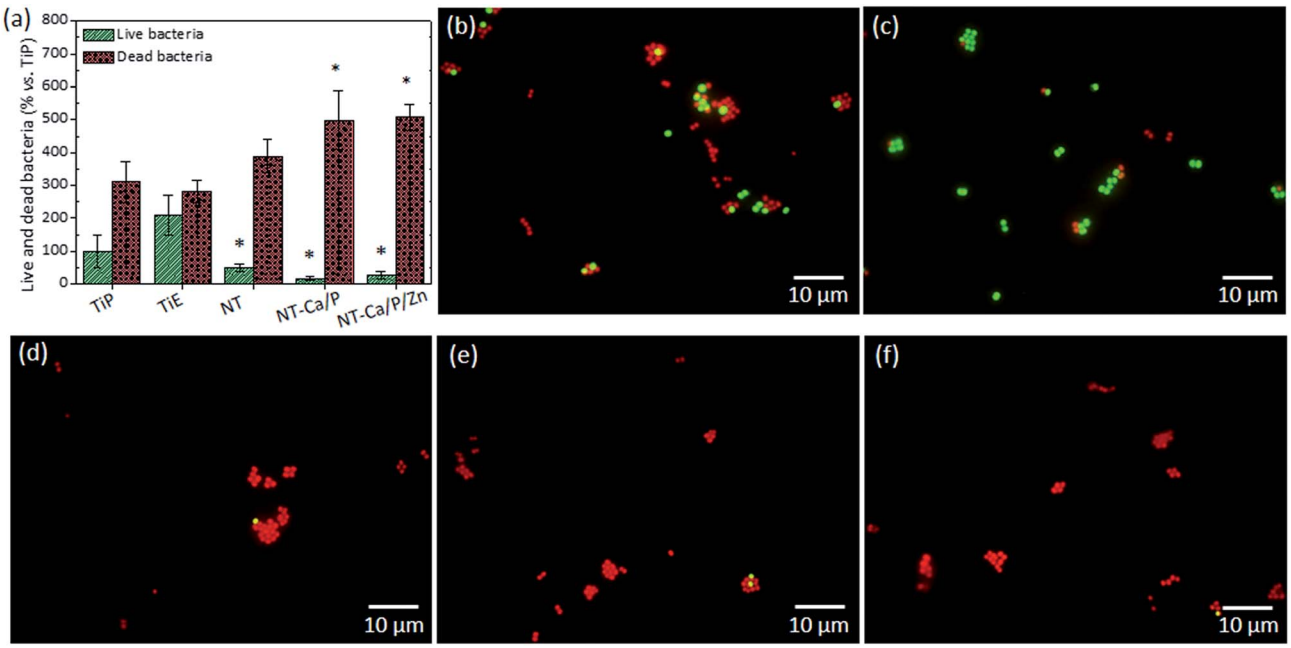


Fig. 9 (a) Live and dead bacteria adhered on TiP, TiE, NT, NT-Ca/P and NT-Ca/P/Zn samples after 2 h of culture. The representative fluorescence images of live (green) and dead (red) adhered bacteria are shown for (b) TiP, (c) TiE, (d) NT, (e) NT-Ca/P and (f) NT-Ca/P/Zn surfaces. For live bacteria: (*) highly significantly different from TiE ($p < 0.001$); for dead bacteria: (*) highly significantly different from TiP and TiE ($p < 0.001$).

Open Access Article. Published on 25 October 2017. Downloaded on 28/10/2017 17:10:08.
This article is licensed under a Creative Commons Attribution 3.0 Unported Licence.

3.3. Microbiological characterization

The influence of materials surface features on the early adhesion and viability of *S. aureus* was investigated, by counting the number of live and dead bacteria adhered to the different groups of surfaces. These results are shown in Fig. 9a, in which the percentage of live and dead bacteria adhered after 2 h of culture is depicted for each group. The number of total live bacteria was converted into a percentage in reference to TiP samples, meaning that the total number of live bacteria counted on TiP samples was taken as 100%. The number of live bacteria adhered on NT, NT-Ca/P and NT-Ca/P/Zn surfaces was significantly lower compared to the number on TiE samples ($p < 0.01$). On the other hand, a significantly higher number of dead bacteria was found on NT-Ca/P and NT-Ca/P/Zn surfaces, when compared to TiP and TiE. The representative images of live (green color) and dead (red color) bacteria adhered on the different groups of surfaces are shown in Fig. 9b–f. In agreement with the previous results, a higher number of live bacteria are observed on TiP and TiE compared to NT, NT-Ca/P and NT-Ca/P/Zn surfaces.

4. Discussion

4.1. Biocompatibility and adhesion ability of MG-63 and hMSCs

The modification of Ti surface features through the creation of micron- to nano-textured surfaces with physicochemical features more compatible with human cells has been adopted as a strategy to improve the performance of dental and orthopedic implants. In particular, various attempts have been made for the development of surfaces mimicking bone structures.[64] At the micron- and nano-scales hierarchical structures of bone, aggregated type-I collagen molecules and hydroxyapatite (HA) crystals form the reinforced collagen fibrils, the universal building elements of both cortical and trabecular bones, providing them flexibility, strength, and toughness. Type-I collagen is a triple helix molecule with ~1.5 nm diameter and ~300 nm length, and plate-shaped HA crystals have 50 × 25 nm in size and 1.5–4 nm thick.[65] Therefore, bone is considered a nanostructured material and efforts have been made to synthesize bone-inspired nano-topographies to enhance biological responses.[3,66] The benefits of the superimposition of micro- and nano-scale topographies on osteoblasts and MSCs functions such as adhesion, proliferation, and differentiation have been reported in previous works.[14,67,68] In the present study, the synthesis of TiO_2 nanotubular surfaces depicted in Fig. 1c intend to mimic such human bone nano-scale features. Besides morphology and topography, the modification of the chemical properties of implant surfaces has demonstrated potential to further improve implant anchorage in bone by rendering the implant surface bioactivity.[69] Therefore, in the current investigation, the TiO_2 nanotubular structures were functionalized with Ca and P elements as $Ca_3(PO_4)_2$ compounds (Fig. 1d), to mimic the mineral composition of natural bone and therefore promote bone regeneration.[70] Additionally, the inclusion of ZnO compounds on nanotubular surfaces was also achieved as shown in Fig. 1e, as the inclusion of Zn on Ti surfaces has been reported to provide osteogenic activity and antibacterial effect.[71,72]

After one day of culture, the enhanced metabolic activity of osteoblast-like cells on TiE samples (Fig. 2a) could have been modulated by the combined micro/nano-topographical surface features (Fig. 1b). Zhao *et al.* (2012)[67] explained that micro/nano topographies may regulate the integrin-mediated cell adhesion process, through several intracellular signal transduction pathways.[73] Nonetheless, the promoter effect of TiE surfaces on cell viability is neither too strong nor long lasting since by day six, the metabolic activity on nanotubular samples is at the same level as that of TiE samples (Fig. 2a), which highlights the biocompatibility of TiO_2 NTs, before and after bio-functionalization treatments. On the other hand, Ti smooth samples keep inducing a significantly lower metabolic activity throughout the culture time, which is most likely related to the absence of either micro or nano topographical cues.

The metabolic activity of hMSCs increased with culture time for all the groups of surfaces (Fig. 4a), however, at a rather limited rate compared to the one observed for MG-63 cells (Fig. 2a). This is probably related with the low metabolic activity of primary hMSCs and their low proliferation rate, when compared to tumoral cells.[74] In addition, it is known that throughout differentiation, the proliferative potential of hMSCs decreases.[75] This also may explain the limited proliferation rate of these cells because, as they were cultured in OM, most likely they were already undergoing a differentiation process at that time.

Both osteoblast-like cells and hMSCs presented very well stretched morphologies when adhered to nanotubular surfaces compared to those of cells on TiP and TiE surfaces (Fig. 2b–f and 4b–f). These differences may be related with the dissimilar features of Ti and nanotubular surfaces, namely their chemistry, surface energy, and nano morphology/topography. These characteristics may play, separately or together, fundamental roles on the initial protein adsorption and subsequent cell adhesion process.[1,76,77] Nano topographical surface features that directly correspond to the sizes of extracellular matrix (ECM) proteins, are known to modulate their initial surface adsorption. Kubo *et al.* (2009)[78] showed the benefits on adding nanonodules on Ti micro-roughened surfaces to boost their capacity of early albumin adsorption. In particular, it is known that the high negative charged density at sharp edges of TiO_2 NTs are expected to promote the adsorption of ECM proteins such as vitronectin, fibronectin, fibrinogen and albumin, which mediates the adsorption of cells to these regions trough integrin receptors present in negatively charged osteoblast membrane surface.[79,80] Nanotubular structures are known to strongly influence the clustering of integrins into focal adhesion complexes, and further activation of intracellular signaling cascades controlling cell adhesion, cell shape, proliferation, migration, differentiation, and apoptosis.[81,82] Although NTs diameters are known to significantly regulate the activation of integrin-mediated intracellular signaling pathways, the optimal range of nanotube diameters to improve cell functions still remains unclear. Controversial results are found in literature,

 This journal is © The Royal Society of Chemistry 2017

Open Access Article. Published on 25 October 2017. Downloaded on 28/10/2017 17:10:08.
This article is licensed under a Creative Commons Attribution 3.0 Unported Licence.

for different studies carried out with 15–150 nm diameter NTs.[19] In the present work, TiO_2 NTs with inner diameters ranging from 50–90 nm and wall thickness comprised between 14 – 24 nm were synthesized.[32] It is believed that the highly stretched morphology observed for MG-63 and hMSC cells on NTs may be related with their non-uniform diameters. Integrins clustering takes place when they are distanced less than 70 nm,[83] and in general, small diameter NTs are known to induce a higher extent of focal adhesion contacts transduced in a stronger cell adhesion and cytoskeleton rearrangement.[79,81,84,85] Based on this knowledge, it is hypothesized that NTs with non-uniform diameters induced the adhesion of proteins in preferential areas of the surfaces, most likely at those places where the density of small-diameter tubes was higher, which consequently might have induced to focal adhesion complexes formation by clustering of integrins at those places. Through activation of intracellular signaling pathways, an increased cytoskeleton stress was probably created inducing cell stretching across the tubes. As observed in Fig. 3d filopodia of cells interacts with NTs by crossing them along their walls, and in general they do not penetrate inside their hollow cavity. This may further indicate that proteins are mainly adsorbed on nanotube wall where cells adhere preferentially.

A dramatic stem cell elongation was also observed by Oh *et al.* (2009)[86] in 100 nm diameter NTs, which induced cytoskeletal stress and differentiation into osteoblasts. The high cytoskeletal tension influences stem cells shape, and their well spreading and stretching across nanotube surfaces predicts their fate towards osteoblast phenotype.[19] In fact, the high cytoskeleton tension may induce to mechanotransduction events and trigger intracellular signaling pathways, which control differentiation.[19,87] However, in this study no correlations were found between the enhanced hMSCs stretching on NTs, and their ability to differentiate into osteoblasts, as it will be further on discussed in more detail.

Different morphologies are observed between filopodia of cells adhered on Ti-based and nanotubular surfaces. As stated by Mattila *et al.* (2008),[88] filopodia are actin-rich plasma membrane protrusions that function as sensors for cells to probe their environment, and are involved in a high number of cell responses such as cell migration and adhesion. In general, osteoblastic-like cells adhered on Ti surfaces present longer and thinner filopodia (Fig. 3a), and their endings display a "ball-like" shape morphology (Fig. 3c). On the contrary, osteoblast-like cells adhered on nanotubular surfaces show shorter and thicker filopodia (Fig. 3b) with flattened endings (Fig. 3d). This is an indicator that MG-63 cells are sensitive to nanotubular surface features, and further suggests that they are stronger adhered to these surfaces. The ability of nanotubular surfaces to strengthen cell adhesion is also suggested by the improved stretching of hMSCs adhered on NTs right after 2 h of adhesion, when compared to the rounder and less stretched morphology of cells adhered on Ti surfaces (Fig. 5). Furthermore, the formation of stress fibers is also observed for hMSCs on nanotubular surfaces, essentially located in cells' endings where well-developed lamellipodia and filopodia are found, through which generally cell spreading occurs.[89] These findings are in accordance with the study performed by Lv *et al.* (2015),[63] who also found that TiO_2 NTs promoted the early adhesion of human stem cells, by accelerating their adhesion as compared to smooth and acid-etched Ti surfaces. Also, Park *et al.* (2007)[81] demonstrated that TiO_2 NTs induced to improved MSC adhesion and spreading as compared to smooth Ti, through focal contact formation and stress fiber assembly.

4.2. Osteogenic differentiation and angiogenic ability of hMSCs

MSCs play a major role in bone formation and regeneration,[45] and their differentiation into mature osteoblasts is comprised by different cellular stages, which are identified by specific markers.[49] Thus, the expression of a series of osteogenic specific genes are involved in osteoblast differentiation and maturation,[90] and some of those important bone markers were addressed in this study.

After 14 days of culture in OM, the expression of BMP-2 was found down-regulated in hMSCs adhered on NT, NT-Ca/P and NT-Ca/P/Zn samples, compared to TiP control (Fig. 7d). Interestingly, although BMP-2 regulates osteogenesis by modulating the expression of RUNX-2,[50,91] which is known as a master regulator of osteogenic gene expression,[90] no link between the down-regulation of BMP-2 and the expression of RUNX-2 was observed (Fig. 7a). Additionally, no correlation between the expression of ALP and COL-1 genes, and the down-regulation of BMP-2 was established (Fig. 7b and c). This may be related with the activation level of RUNX-2, which is not being influenced by BMP-2. RUNX-2 is an important transcriptional factor needed for the osteoblast lineage commitment, and further modulation of osteoblast differentiation, bone development, and the expression of ECM protein genes.[50,51,90,92] In the earliest stage, MSCs form pre-osteoblasts that secrete ALP, an early marker of osteogenesis,[50] while in a later stage mature osteoblasts secrete bone organic matrix rich in COL-1, which afterwards become mineralized through hydroxyapatite deposition.[49] The expression of ALP and COL-1 present similar levels for hMSCs cultured both on Ti and nanotubular surfaces, suggesting that osteogenic differentiation is not being compromised by surface modification treatments induced on Ti surfaces. As regards the lower expression of BMP-2 in cells cultured on nanotubular surfaces, no correlation was found with the increased cell stretching observed for these cells, as previously described. Studies found in literature show the reverse trend, since cell stretching stress is reported to induce osteogenic differentiation of stem cells.[67,93–95] A possible explanation for this behavior may be related with surface chemistry, which is different for all the nanotubular surfaces as compared to Ti surfaces. The presence of fluoride ions adsorbed to TiO_2 NTs were found on all the nanotubular surfaces (Fig. 1c), and previous studies have reported that fluoride regulate osteoblastic differentiation.[96–98] A recent study conducted by Gandhi *et al.* (2017)[97] showed that fluoride induced chronic oxidative and inflammatory stress in osteoblast-like cells, which was highlighted to possibly hamper osteoblast differentiation. Furthermore, Zhao *et al.* (2016)[96] found that fluoride inhibited BMP-2 expression levels in rat

Open Access Article. Published on 25 October 2017. Downloaded on 28/10/2017 17:10:08.
This article is licensed under a Creative Commons Attribution 3.0 Unported Licence.

osteoblasts. Thus, the presence of fluoride on TiO_2 nanotubular surfaces may be a possible reason for the reduced BMP-2 levels.

Remarkably, the expression levels of OPN followed the same trend of BMP-2 for NT and NT-Ca/P samples, in which OPN gene was down-regulated compared to Ti smooth and rough surfaces (Fig. 7d and e). This suggests that the regulation of OPN gene is being influenced by BMP-2. In fact, some reports have mentioned that BMP-2 regulates the cellular gene expression of OPN,[99–101] however, the mechanisms behind still remain unclear. It is known that the BMP signaling pathway plays multiple and crucial roles in bone formation and is involved in several stages of its development.[50] The stimulation of the differentiation of MSCs into osteoblasts through BMP-2 is mainly achieved through stimulating Smad signaling pathway. By activating Smad-1/5/8 and RUNX-2, BMP-2 regulates the expression of osteoblastic-specific genes such as OPN, a late osteogenic marker.[50,51,91] Yang *et al.* (2009)[101] studied the role of BMP-2 on the enhancement of RUNX-2 and OPN expression by Smad-1 and signal-related kinase (ERK) 1/2 signaling pathways, and concluded that extracellular ERK 1/2 pathway modulates BMP-2-induced OPN expression. Thus, it is believed that Smad and/or ERK 1/2 are the most probable pathways involved in the control of OPN expression by BMP-2. However, further studies must be performed to clarify this hypothesis.

Besides gene expression levels of BMP-2 and OPN have been found down-regulated in cells cultured on nanotubular surfaces compared to TiP, these genes were significantly up-regulated on TiO_2 nanotubular surfaces enriched with ZnO compounds (Fig. 1e), when compared to NT and NT-Ca/P surfaces (insertions in Fig. 7d and e). This suggests that the inclusion of Zn on TiO_2 NTs is enhancing the osteoblastic differentiation of hMSCs. It is known that Zn ions (Zn^{2+}) concentration is relatively high in bone and it has been propose to stimulate bone formation and mineralization.[39] Previous studies have demonstrated that Zn plays an important role in differentiation of osteoblasts and bone remodeling. Recently, Yusa *et al.* (2016)[41] demonstrated that Zn-modified Ti surface enhances osteoblast differentiation of dental pulp stem cells. The authors reported that Zn–Ti surfaces, beyond exhibited significantly up-regulated gene expression levels of BMP-2, OPN, RUNX-2, ALP, and COL-1, also promoted ECM mineralization. Additionally, it is suggested that the improved osteogenic-genes expression in Zn–Ti surfaces was linked to the activation of Smad-1/5/8. In particular, the enrichment of TiO_2 NTs with Zn has shown promising results by improving osseointegration both *in vitro* and *in vivo*.[40] For example, Huo *et al.* (2013)[33] reported that the incorporation of Zn on nanotube arrays showed excellent osteogenesis inducing ability through higher activity of extracellular ERK 1/2, which is one of the alternative pathways (non-Smad dependent pathway) that regulates osteogenic differentiation of stem cells.[102] These finding are in accordance with recent discoveries reporting that Zn^{2+} ions regulate several intracellular signaling pathways including BMP-2 signaling cascade. It is believed that intracellular influx of Zn^{2+} ions is controlled by Zn transporters involved in bone homeostasis.[39] Based on these findings, it is hypothesized that Zn^{2+} ions liberated from NT-Ca/P/Zn samples reaches the intracellular environment through Zn specific transporters, and by this way may enhance the activity of intracellular signaling pathways involved in osteogenic differentiation, including Smad and/or ERK 1/2. As previously mentioned, BMP-2 is known to promote osteoblast differentiation and OPN is a mature osteoblast marker gene recognized to play an important role in bone formation, resorption, and remodeling.[41,52] By enhancing the BMP-2 and OPN levels, the addition of Zn on nanotubular surfaces seems be of crucial importance to act as a potent inducer of bone formation and remodeling.

As regards hMSCs adhered on nanotubular surfaces, although not statistically significant, a trend is observed for a gradual decrease in the metabolic activity of cells adhered on those bio-functionalized samples as compared to conventional NTs, both after one and six days of culture (Fig. 4a). A lower metabolic activity is indicator of a lower proliferation rate, and this is agreement with the interrelation found between proliferation and differentiation of cells during development of osteoblast phenotype.[14] This slight suppressive effect of metabolic activity is possibly related to hMSCs differentiation tendency found for bio-functionalized NTs, in particular those containing Zn. However, the micro/nano scale surface topography of TiE samples seems to result in an additive effect on hMSCs metabolic activity, when compared to NT-Ca/P and NT-Ca/P/Zn samples (day one), and after six days this difference become only significant for NT-Ca/P/Zn samples. Nevertheless, nanotubular samples are shown to support MSC proliferation and do not compromise their viability, as the values are never lower than that of the well-known biocompatible Ti smooth surfaces. The stronger adhesion strength of cells adhered on nanotubular surfaces may also be related with the lower proliferation rate since, as explained by Zhao *et al.* (2012),[67] as cells need to detach slightly to undergo division, a tight adhesion is expected to hamper this process.

Bone is a highly vascularized tissue, and blood vessels largely contribute for bone growth and remodeling.[103,104] Therefore, vasculogenesis and angiogenesis processes are required for proper osseointegration. Vascular endothelial growth factor (VEGF) is among the many identified growth factors that initiates and controls angiogenesis.[105] The amount of VEGF produced by hMSCs after 14 days of incubation in OM, was found to be significantly higher for NT and NT-Ca/P/Zn surfaces compared to TiP and TiE surfaces (Fig. 8). Moreover, hMSCs on NT-Ca/P surfaces released a significantly higher amount of VEGF in relation to TiE, although these differences were found not significant when compared to TiP surfaces. These results may be related with the morphological/topographical and physicochemical properties of the surfaces. In previous studies, surface topography and surface energy were found to regulate the secretion of angiogenic factors by cells, partially *via* $\alpha_2\beta_1$ integrin signaling.[105,106] TiO_2 nanotubular surfaces, in addition to nanotopography, are more hydrophilic (higher surface energy[63]) compared to Ti surfaces (results not shown). Thus, it is believed that both nanotopography and physicochemical features of nanotubular surfaces are influencing the synthesis of VEGF, probably mediated by integrin signaling pathways. Although not statistically significant, there is a trend for a lower

Open Access Article. Published on 25 October 2017. Downloaded on 28/10/2017 17:10:08.
This article is licensed under a Creative Commons Attribution 3.0 Unported Licence.

VEGF production by cells in contact with NT-Ca/P, as compared to NT and NT-Ca/P/Zn surfaces. However, no relation has been found between VEGF synthesis and the presence of Ca, which is the main difference existing between the surfaces. One must be highlighted that VEGF and BMP-2 play important roles in the communication between osteogenesis and angiogenesis.[106] In accordance with previous studies, the production of VEGF by osteoblasts is regulated by factors that stimulate osteogenesis, including BMP-2.[105,107] Based on this knowledge, we postulate that the lower expression level of BMP-2 gene for NT surfaces is not compromising the synthesis of VEGF.

4.3. Early bacterial adhesion and survival on Ti and nanotubular surfaces

In addition to complicated infections, bacterial adhesion on implant surfaces may compromise the osseointegration process.[1] In this study, the early adhesion of *S. aureus* on Ti and nanotubular surfaces was investigated. The main aim was to understand the influence of the surface features on bacterial adhesion, as well as infer on their ability to impair their viability.

In this study, a significantly higher number of live bacteria was adhered on TiE surfaces compared to NT, NT-Ca/P and NT-Ca/P/Zn surfaces (Fig. 9). One of the main differences between theses surfaces is the micro/nano topography of TiE surfaces. As compared to smooth surfaces, roughened substrates have demonstrated potential to enhance the adhesion and growth of infectious bacteria.[15,64,108–110] Wu *et al.* (2011)[15] studied the effects of surface topography on *S. epidermidis* using clinically relevant Ti surface finishes, and they found that bacterial adhesion and growth was substantially higher on rough ($0.830\ \mu m < R_a < 11\ \mu m$) surfaces than on the Ti polished ($R_a = 0.006\ \mu m$) surfaces after 24 h of culture. The observed differences were linked to the substantially higher roughness of the former surfaces at lengths scales comparable to that of bacterial colonies (several microns). Whitehead *et al.* (2005)[111] also studied the adhesion of bacteria on substrates with micrometer and sub-micrometer dimensions, and found that *S. aureus* and *Pseudomonas aeruginosa* (*P. aeruginosa*) were retained mainly in the largest (2 μm) surface features. On the other hand, i*n vitro* antibacterial properties of nanostructured Ti surfaces have been demonstrated by several studies.[24,112,113] Puckett *et al.* (2010)[114] examined the adhesion of *S. aureus*, *S. epidermidis*, and *P. aeruginosa* on conventional Ti (nano-smooth) and nanostructured Ti surfaces after 1 h of culture. The results indicated that nanorough Ti surfaces are the best surfaces for inhibiting bacterial adhesion. The authors explained that the decreased bacterial attachment was related with the higher surface energy of nanostructured Ti surfaces which increased fibronectin adsorption, and subsequently decreased bacteria attachment. The above mentioned studies suggest that while micron-roughened Ti substrates show potential to enhance the adhesion and growth of bacteria, nanostructured Ti surfaces display the reverse trend.

An additional interesting outcome in this investigation is related with the remarkably higher number of dead bacteria on NT-Ca/P and NT-Ca/P/Zn surfaces, when compared to TiP and TiE surfaces. These results suggest that TiO_2 nanotubular surfaces display the ability to impair bacterial functions in respect to their viability. Ercan *et al.* (2011)[24] also found that TiO_2 nanotubular structures reduced the number of live adhering *S. epidermidis* and *S. aureus*. However, the mechanisms behind such strong bactericidal effect of TiO_2 NTs are still poorly understood, and controversial results are found in literature. Antimicrobial properties of TiO_2 NTs are reported to be related mainly to the following mechanisms: (1) formation of reactive oxygen species (ROS) in bacteria;[112] (2) disruption of bacteria membrane due to stress effects induced by NTs;[24] and (3) oxidative stress induced by photocatalytic activity of TiO_2.[113] In fact, the topographical cues of TiO_2 NTs may be one of the reasons for the lower bacterial viability. Kang *et al.* (2007)[115] reported that bacterial cell membrane damage resulting from direct contact with single-walled carbon NTs is the probable mechanism leading to bacterial cell death. This mechanism was also addressed by Shi *et al.* (2015)[25] to explain the increased antibacterial activity of TiO_2 NTs with diameters ranging from 30–60 nm. The authors suggested that physical contact of bacteria with NTs could induce a punch on bacteria with cell membrane ruptures and cytoplasm outflow, leading eventually to cell apoptosis.

Beyond morphological/topographical characteristics, all the nanotubular surfaces present different chemical features as compared to Ti surfaces. These surfaces beyond TiO_2, which is also present on Ti surfaces, are composed of adsorbed fluoride ions (Fig. 1c), which can inhibit the metabolism and growth of bacteria. Breaker (2012)[116] reported that bacteria such as *Escherichia coli* or fungi such as *Candida albicans* cannot survive upon long exposure to fluoride approaching 250 mM, the concentration found in some fluoride toothpastes. It is believed that fluoride can affect bacterial metabolism through a set of actions and different mechanisms such as acting directly as an enzyme inhibitor.[117] Recently, Liu *et al.* (2016)[118] reported that the incorporation of fluoride ions into bioactive glasses significantly promoted the antimicrobial activity against periodontal pathogens. Thus, the mechanism behind the bactericidal activity of nanotubular surfaces compared to Ti may be also related with fluoride action by inhibiting enzymatic activity of bacteria. Furthermore, although not statistically significant, the number of live and dead bacteria adhered on NT-Ca/P and NT-Ca/P/Zn surfaces was found lower and higher, respectively, when compared to bacteria adhered on NT surfaces (Fig. 9), suggesting that Ca, P and Zn may also influence bacteria viability. However, further studies should be performed to better understand the simultaneous action of topographical and physicochemical features of TiO_2 NTs, on the significant decrease and increase of live and dead adhered bacteria, respectively.

5. Conclusions

TiO_2 NTs enriched with Ca, P and Zn were successfully synthesized by reverse polarization anodization treatments carried out over conventional TiO_2 nanotubular surfaces. The

Open Access Article. Published on 25 October 2017. Downloaded on 28/10/2017 17:10:08.
This article is licensed under a Creative Commons Attribution 3.0 Unported Licence.



influence of bio-functionalized TiO_2 NTs on the biological performance of MG-63 and hMSCs cells was investigated, together with their ability to display antimicrobial properties. Henceforward the main outcomes of this study are highlighted:

– Bio-functionalized TiO_2 nanotubular surfaces are biocompatible for MG-63 cells and hMSCs. Furthermore, TiO_2 NTs modulated the morphology of MG-63 cells and hMSCs, which presented a more stretched morphology compared to Ti smooth and rough surfaces.

– The expression of BMP-2 was found down-regulated in hMSCs adhered on conventional TiO_2 NTs compared to Ti, which was reflected in a down-regulation of OPN.

– OPN gene expression is probably regulated by BMP-2 levels: the enrichment of TiO_2 nanotubular surfaces with Ca, P and Zn significantly enhanced the expression of BMP-2, which was reflected in the up-regulation of OPN.

– All TiO_2 nanotubular surfaces induced the release of significantly higher amount of VEGF as compared to smooth and micro/nano-roughened Ti surfaces;

– TiO_2 NTs, before and after bio-functionalization, induced a significant reduction in the number of live bacteria as compared to Ti surfaces.

Taking together the enhanced BMP-2 and OPN expression levels along with the higher amount of VEGF produced, these results suggest that the combined effect of TiO_2 nanotubular-textured surfaces with the surface enrichment with Ca, P, and Zn, is a very promising approach to promote bone formation, remodeling and vascularization processes, thereby improving implant osseointegration. Simultaneously, these surfaces display antimicrobial properties coming up with new insights for the development of efficient bio-selective surfaces for osseointegrated implants applications.

Conflicts of interest

There are no conflicts of interest to declare.

Acknowledgements

The authors acknowledge the financial support from FCT by the doctoral grant (Ref. SFRH/BD/88517/2012), CAPES (Proc. 99999.008666/2014-08), CNPq (Proc. 490761/2013-5) and UNESP. Also, the authors would like to thank Rio de Janeiro cell bank (BCRJ, Rio de Janeiro, Brasil) for all the support provided for biological experiments, as well Fernando Almeida for technical assistance at confocal microscope in CENABIO-UFRJ (Rio de Janeiro, Brasil). Tolou Shokuhfar especially thanks to US National Science Foundation NSF-DMR CAREER award # 1564950.

References

1 K. G. Neoh, X. Hu, D. Zheng and E. T. Kang, *Biomaterials*, 2012, **33**, 2813–2822.
2 D.-W. Lee, Y.-P. Yun, K. Park and S. E. Kim, *Bone*, 2012, **50**, 974–982.
3 C. Yao and T. J. Webster, *J. Nanosci. Nanotechnol.*, 2006, **6**, 2682–2692.
4 M. Ribeiro, F. J. Monteiro and M. P. Ferraz, *Biomatter*, 2012, **2**, 176–194.
5 J. Raphel, M. Holodniy, S. B. Goodman and S. C. Heilshorn, *Biomaterials*, 2016, **84**, 301–314.
6 D. W. Paquette, N. Brodala and R. C. Williams, *Dent. Clin. North Am.*, 2006, **50**, 361–374.
7 K. Gulati, S. Ramakrishnan, M. S. Aw, G. J. Atkins, D. M. Findlay and D. Losic, *Acta Biomater.*, 2012, **8**, 449–456.
8 G. Subbiahdoss, R. Kuijer, D. W. Grijpma, H. C. van der Mei and H. J. Busscher, *Acta Biomater.*, 2009, **5**, 1399–1404.
9 E. Abt, J. W. Hellstein, P. B. Lockhart, A. J. Mariotti, T. P. Sollecito, E. L. Truelove, S. Armstrong, S. S. De Rossi, J. B. Epstein and J. M. Laudenbach, *J. Am. Dent. Assoc., JADA*, 2017, **2**, 57–59.
10 S. Landgraeber, M. Jäger, J. J. Jacobs and N. J. Hallab, *Mediators Inflammation*, 2014, **2014**, 1–9.
11 D. Schwartz-Arad, A. Laviv and L. Levin, *Implant Dent.*, 2008, **17**, 200–207.
12 M. Srinivasan, S. Meyer, A. Mombelli and F. Müller, *Clin. Oral Implants Res.*, 2016, 1–11.
13 H. V. Cruz, J. C. M. Souza, M. Henriques and L. A. Rocha, in *Biomedical Tribology*, ed. J. P. Davim, Nova Science Publishers, 2011, pp. 1–30.
14 R. A. Gittens, T. McLachlan, R. Olivares-Navarrete, Y. Cai, S. Berner, R. Tannenbaum, Z. Schwartz, K. H. Sandhage and B. D. Boyan, *Biomaterials*, 2011, **32**, 3395–3403.
15 Y. Wu, J. P. Zitelli, K. S. TenHuisen, X. Yu and M. R. Libera, *Biomaterials*, 2011, **32**, 951–960.
16 S. Alves, R. Bayón, V. S. de Viteri, M. Garcia, A. Igartua, M. Fernandes and L. Rocha, *Journal of Bio -and Tribo-Corrosion*, 2015, **1**, 23.
17 C.-Y. Chiang, S.-H. Chiou, W.-E. Yang, M.-L. Hsu, M.-C. Yung, M.-L. Tsai, L.-K. Chen and H.-H. Huang, *Dent. Mater.*, 2009, **25**, 1022–1029.
18 S. Svensson, F. Suska, L. Emanuelsson, A. Palmquist, B. Norlindh, M. Trobos, H. Bäckros, L. Persson, G. Rydja, M. Ohrlander, B. Lyvén, J. Lausmaa and P. Thomsen, *Nanomedicine*, 2013, **9**, 1048–1056.
19 K. S. Brammer, C. J. Frandsen and S. Jin, *Trends Biotechnol.*, 2012, **30**, 315–322.
20 S. Oh, C. Daraio, L.-H. Chen, T. R. Pisanic, R. R. Fiñones and S. Jin, *J. Biomed. Mater. Res., Part A*, 2006, **78**, 97–103.
21 L. M. Bjursten, L. Rasmusson, S. Oh, G. C. Smith, K. S. Brammer and S. Jin, *J. Biomed. Mater. Res., Part A*, 2010, **92**, 1218–1224.
22 T. Shokuhfar, A. Hamlekhan, J.-Y. Chang, C. K. Choi, C. Sukotjo and C. Friedrich, *Int. J. Nanomed.*, 2014, **9**, 3737.
23 A. Rajyalakshmi, B. Ercan, K. Balasubramanian and T. J. Webster, *Int. J. Nanomed.*, 2011, **2011**, 1765–1771.
24 B. Ercan, E. Taylor, E. Alpaslan and T. J. Webster, *Nanotechnology*, 2011, **22**, 295102.
25 X. Shi, Q. Xu, A. Tian, Y. Tian, X. Xue, H. Sun, H. Yang and C. Dong, *RSC Adv.*, 2015, **5**, 34237–34242.

 This journal is © The Royal Society of Chemistry 2017

Open Access Article. Published on 25 October 2017. Downloaded on 28/10/2017 17:10:08.
This article is licensed under a Creative Commons Attribution 3.0 Unported Licence.

26 Y. Zhao, Q. Xing, J. Janjanam, K. He, F. Long, K.-B. Low, A. Tiwari, F. Zhao, R. Shahbazian-Yassar and C. Friedrich, *Int. J. Nanomed.*, 2014, **9**, 5177.
27 A. Gao, R. Hang, X. Huang, L. Zhao, X. Zhang, L. Wang, B. Tang, S. Ma and P. K. Chu, *Biomaterials*, 2014, **35**, 4223–4235.
28 C. Xie, P. Li, Y. Liu, F. Luo and X. Xiao, *Mater. Sci. Eng., C*, 2016, **67**, 433–439.
29 J. Chen, Z. Zhang, J. Ouyang, X. Chen, Z. Xu and X. Sun, *Appl. Surf. Sci.*, 2014, **305**, 24–32.
30 L. Zhao, H. Wang, K. Huo, L. Cui, W. Zhang, H. Ni, Y. Zhang, Z. Wu and P. K. Chu, *Biomaterials*, 2011, **32**, 5706–5716.
31 Y. Hu, K. Cai, Z. Luo, D. Xu, D. Xie, Y. Huang, W. Yang and P. Liu, *Acta Biomater.*, 2012, **8**, 439–448.
32 S. A. Alves, S. B. Patel, C. Sukotjo, M. T. Mathew, N. Paulo Filho, J.-P. Celis, L. A. Rocha and T. Shokuhfar, *Appl. Surf. Sci.*, 2017, **399**, 682–701.
33 K. Huo, X. Zhang, H. Wang, L. Zhao, X. Liu and P. K. Chu, *Biomaterials*, 2013, **34**, 3467–3478.
34 H. Yazici, H. Fong, B. Wilson, E. Oren, F. Amos, H. Zhang, J. Evans, M. Snead, M. Sarikaya and C. Tamerler, *Acta Biomater.*, 2013, **9**, 5341–5352.
35 A. Roguska, M. Pisarek, M. Andrzejczuk, M. Dolata, M. Lewandowska and M. Janik-Czachor, *Mater. Sci. Eng., C*, 2011, **31**, 906–914.
36 T. Shokuhfar, S. Sinha-Ray, C. Sukotjo and A. L. Yarin, *RSC Adv.*, 2013, **3**, 17380–17386.
37 A. Hamlekhan, S. Sinha-Ray, C. Takoudis, M. T. Mathew, C. Sukotjo, A. L. Yarin and T. Shokuhfar, *J. Phys. D: Appl. Phys.*, 2015, **48**, 275401.
38 K. Gulati, M. S. Aw and D. Losic, *Nanoscale Res. Lett.*, 2011, **6**, 571.
39 T. Fukada, S. Hojyo and T. Furuichi, *J. Bone Miner. Metab.*, 2013, **31**, 129–135.
40 Y. Li, W. Xiong, C. Zhang, B. Gao, H. Guan, H. Cheng, J. Fu and F. Li, *J. Biomed. Mater. Res., Part A*, 2014, **102**, 3939–3950.
41 K. Yusa, O. Yamamoto, H. Takano, M. Fukuda and M. Iino, *Sci. Rep.*, 2016, **6**, 29462.
42 S. A. Alves, A. L. Rossi, A. R. Ribeiro, J. Werckmann, J.-P. Celis, L. A. Rocha and T. Shokuhfar, *Surf. Coat. Technol.*, 2017, **324**, 153–166.
43 S. A. Alves, A. L. Rossi, A. R. Ribeiro, F. Toptan, A. M. Pinto, J.-P. Celis, T. Shokuhfar and L. A. Rocha, *Wear*, 2017, **384**, 28–42.
44 C. Pautke, M. Schieker, T. Tischer, A. Kolk, P. Neth, W. Mutschler and S. Milz, *Anticancer Res.*, 2004, **24**, 3743–3748.
45 K. H. Kraus and C. Kirker-Head, *Vet. Surg.*, 2006, **35**, 232–242.
46 P. Falagan-Lotsch, T. S. Lopes, N. Ferreira, N. Balthazar, A. M. Monteiro, R. Borojevic and J. M. Granjeiro, *J. Microbiol. Methods*, 2015, **118**, 31–36.
47 B. Cosme, P. Falagan-Lotsch, M. Ribeiro, K. Napoleão, J. M. Granjeiro and R. Moura-Neto, *In Vitro Cell. Dev. Biol.: Anim.*, 2017, 1–5.
48 T. L. Riss, R. A. Moravec, A. L. Niles, H. A. Benink, T. J. Worzella and L. Minor, in *Assay Guidance Manual [Internet]*, ed. G. S. Sittampalam, N. P. Coussens, K. Brimacombe, *et al.*, Eli Lilly & Company and the National Center for Advancing Translational Sciences, 2016.
49 N. Dirckx, M. Hul and C. Maes, *Birth Defects Res., Part C*, 2013, **99**, 170–191.
50 M. Beederman, J. D. Lamplot, G. Nan, J. Wang, X. Liu, L. Yin, R. Li, W. Shui, H. Zhang and S. H. Kim, *J. Biomed. Sci. Eng.*, 2013, **6**, 32.
51 J. Yang, P. Shi, M. Tu, Y. Wang, M. Liu, F. Fan and M. Du, *Food Science and Human Wellness*, 2014, **3**, 127–135.
52 K. Terai, T. Takano-Yamamoto, Y. Ohba, K. Hiura, M. Sugimoto, M. Sato, H. Kawahata, N. Inaguma, Y. Kitamura and S. Nomura, *J. Bone Miner. Res.*, 1999, **14**, 839–849.
53 W. C. Rodrigues, A. L. da Silva Fabris, J. S. Hassumi, A. Gonçalves, C. K. Sonoda and R. Okamoto, *Br. J. Oral Maxillofac. Surg.*, 2016, **54**, 531–535.
54 K. J. Livak and T. D. Schmittgen, *methods*, 2001, **25**, 402–408.
55 R. P. Antony, T. Mathews, S. Dash, A. K. Tyagi and B. Raj, *Mater. Chem. Phys.*, 2012, **132**, 957–966.
56 D. Regonini, A. Jaroenworaluck, R. Stevens and C. R. Bowen, *Surf. Interface Anal.*, 2010, **42**, 139–144.
57 M. Pisarek, A. Roguska, L. Marcon and M. Andrzejczuk, *Biomimetic and Electrodeposited Calcium-Phosphates Coatings on Ti – Formation, Surface Characterization, Biological Response*, INTECH Open Access Publisher, 2012.
58 B.-S. Kang, Y.-T. Sul, S.-J. Oh, H.-J. Lee and T. Albrektsson, *Acta Biomater.*, 2009, **5**, 2222–2229.
59 K. Indira, U. K. Mudali and N. Rajendran, *J. Biomater. Appl.*, 2014, **29**, 113–129.
60 W. Fu, S. Ding, Y. Wang, L. Wu, D. Zhang, Z. Pan, R. Wang, Z. Zhang and S. Qiu, *Dalton Trans.*, 2014, **43**, 16160–16163.
61 D.-B. Lee, L.-S. Hong and Y.-J. Kim, *Mater. Trans.*, 2008, **49**, 1084–1088.
62 Y. Tanaka, H. Saito, Y. Tsutsumi, H. Doi, H. Imai and T. Hanawa, *Mater. Trans.*, 2008, **49**, 805–811.
63 L. Lv, Y. Liu, P. Zhang, X. Zhang, J. Liu, T. Chen, P. Su, H. Li and Y. Zhou, *Biomaterials*, 2015, **39**, 193–205.
64 K. Anselme, P. Davidson, A. Popa, M. Giazzon, M. Liley and L. Ploux, *Acta Biomater.*, 2010, **6**, 3824–3846.
65 X. Wang, S. Xu, S. Zhou, W. Xu, M. Leary, P. Choong, M. Qian, M. Brandt and Y. M. Xie, *Biomaterials*, 2016, **83**, 127–141.
66 E. Palin, H. Liu and T. J. Webster, *Nanotechnology*, 2005, **16**, 1828.
67 L. Zhao, L. Liu, Z. Wu, Y. Zhang and P. K. Chu, *Biomaterials*, 2012, **33**, 2629–2641.
68 L. Zhao, S. Mei, P. K. Chu, Y. Zhang and Z. Wu, *Biomaterials*, 2010, **31**, 5072–5082.
69 L. Le Guéhennec, A. Soueidan, P. Layrolle and Y. Amouriq, *Dent. Mater.*, 2007, **23**, 844–854.
70 R. A. Surmenev, M. A. Surmeneva and A. A. Ivanova, *Acta Biomater.*, 2014, **10**, 557–579.

Open Access Article. Published on 25 October 2017. Downloaded on 28/10/2017 17:10:08.
This article is licensed under a Creative Commons Attribution 3.0 Unported Licence.

71 Y. Qiao, W. Zhang, P. Tian, F. Meng, H. Zhu, X. Jiang, X. Liu and P. K. Chu, *Biomaterials*, 2014, **35**, 6882–6897.
72 G. Jin, H. Cao, Y. Qiao, F. Meng, H. Zhu and X. Liu, *Colloids Surf., B*, 2014, **117**, 158–165.
73 E. J. Kim, C. A. Boehm, A. Mata, A. J. Fleischman, G. F. Muschler and S. Roy, *Acta Biomater.*, 2010, **6**, 160–169.
74 B. Heidari, A. Shirazi, M. M. Akhondi, H. Hassanpour, B. Behzadi, M. M. Naderi, A. Sarvari and S. Borjian, *Avicenna J. Med. Biotechnol.*, 2013, **5**, 104–117.
75 D. Baksh, L. Song and R. Tuan, *J. Cell. Mol. Med.*, 2004, **8**, 301–316.
76 A. Chug, S. Shukla, L. Mahesh and S. Jadwani, *J. Oral Maxillofac. Surg. Med. Pathol.*, 2013, **25**, 1–4.
77 W. Singhatanadgit, *Bone Tissue Regener. Insights*, 2009, **2**, 1–11.
78 K. Kubo, N. Tsukimura, F. Iwasa, T. Ueno, L. Saruwatari, H. Aita, W.-A. Chiou and T. Ogawa, *Biomaterials*, 2009, **30**, 5319–5329.
79 M. Kulkarni, A. Mazare, E. Gongadze, Š. Perutkova, V. Kralj-Iglič, I. Milošev, P. Schmuki, A. Iglič and M. Mozetič, *Nanotechnology*, 2015, **26**, 062002.
80 M. Pegueroles, C. Tonda-Turo, J. A. Planell, F.-J. Gil and C. Aparicio, *Biointerphases*, 2012, **7**, 1–13.
81 J. Park, S. Bauer, K. von der Mark and P. Schmuki, *Nano Lett.*, 2007, **7**, 1686–1691.
82 W. F. Zambuzzi, P. G. Coelho, G. G. Alves and J. M. Granjeiro, *Biotechnol. Bioeng.*, 2011, **108**, 1246–1250.
83 A. T. Nguyen, S. R. Sathe and E. K. Yim, *J. Phys.: Condens. Matter*, 2016, **28**, 183001.
84 S. Bauer, J. Park, J. Faltenbacher, S. Berger, K. von der Mark and P. Schmuki, *Integr. Biol.*, 2009, **1**, 525–532.
85 R. Imani, D. Kabaso, M. Erdani Kreft, E. Gongadze, S. Penič, K. Eleršič, A. Kos, P. Veranič, R. Zorec and A. Iglič, *Croat. Med. J.*, 2012, **53**, 577–585.
86 S. Oh, K. S. Brammer, Y. S. J. Li, D. Teng, A. J. Engler, S. Chien and S. Jin, *Proc. Natl. Acad. Sci. U. S. A.*, 2009, **106**, 2130–2135.
87 Y. R. V. Shih, K. F. Tseng, H. Y. Lai, C. H. Lin and O. K. Lee, *J. Bone Miner. Res.*, 2011, **26**, 730–738.
88 P. K. Mattila and P. Lappalainen, *Nat. Rev. Mol. Cell Biol.*, 2008, **9**, 446–454.
89 A. Tian, X. Qin, A. Wu, H. Zhang, Q. Xu, D. Xing, H. Yang, B. Qiu, X. Xue and D. Zhang, *Int. J. Nanomed.*, 2015, **10**, 2423.
90 X. Zheng, F. Zhou, Y. Gu, X. Duan and A. Mo, *Sci. Rep.*, 2017, **7**, 41945.
91 Y.-K. Wang, X. Yu, D. M. Cohen, M. A. Wozniak, M. T. Yang, L. Gao, J. Eyckmans and C. S. Chen, *Stem Cells Dev.*, 2011, **21**, 1176–1186.
92 T. Komori, *Cell Tissue Res.*, 2010, **339**, 189.
93 R. Li, L. Liang, Y. Dou, Z. Huang, H. Mo, Y. Wang and B. Yu, *BioMed Res. Int.*, 2015, **2015**, 1–10.
94 X. Yang, P. Gong, Y. Lin, L. Zhang, X. Li, Q. Yuan, Z. Tan, Y. Wang, Y. Man and H. Tang, *Arch. Med. Sci.*, 2010, **6**, 152–159.
95 B. E. Grottkau, X. Yang, L. Zhang, L. Ye and Y. Lin, *Bone Res.*, 2013, **1**, 282–290.
96 Y. Zhao, M. Huo, Y. Liu, Y. Xie, J. Wang, Y. Li and J. Wang, *Fluoride*, 2016, **49**, 13–22.
97 D. Gandhi, P. K. Naoghare, A. Bafana, K. Kannan and S. Sivanesan, *Biol. Trace Elem. Res.*, 2017, **175**, 103–111.
98 C. Yang, Y. Wang and H. Xu, *PLoS One*, 2017, **12**, e0170674.
99 J. Sun, J. Li, C. Li and Y. Yu, *Mol. Med. Rep.*, 2015, **12**, 4230–4237.
100 T. Schwarting, D. Schenk, M. Frink, M. Benölken, F. Steindor, M. Oswald, S. Ruchholtz and P. Lechler, *Connect. Tissue Res.*, 2016, **57**, 99–112.
101 X. Yang, X. Meng, X. Su, D. C. Mauchley, L. Ao, J. C. Cleveland Jr and D. A. Fullerton, *J. Thorac. Cardiovasc. Surg.*, 2009, **138**, 1008–1015.
102 M. Wu, G. Chen and Y.-P. Li, *Bone Res.*, 2016, **4**, 16009.
103 U. Saran, S. G. Piperni and S. Chatterjee, *Arch. Biochem. Biophys.*, 2014, **561**, 109–117.
104 V. Veeriah, A. Zanniti, R. Paone, S. Chatterjee, N. Rucci, A. Teti and M. Capulli, *Sci. Rep.*, 2016, **6**, 29880.
105 A. L. Raines, R. Olivares-Navarrete, M. Wieland, D. L. Cochran, Z. Schwartz and B. D. Boyan, *Biomaterials*, 2010, **31**, 4909–4917.
106 L. Bai, R. Wu, Y. Wang, X. Wang, X. Zhang, X. Huang, L. Qin, R. Hang, L. Zhao and B. Tang, *J. Mater. Chem. B*, 2016, **4**, 5548–5559.
107 M. M. Deckers, R. L. Van Bezooijen, G. Van Der Horst, J. Hoogendam, C. van der Bent, S. E. Papapoulos and C. W. Löwik, *Endocrinology*, 2002, **143**, 1545–1553.
108 K. Hori and S. Matsumoto, *Biochem. Eng. J.*, 2010, **48**, 424–434.
109 A. Han, J. K. H. Tsoi, F. P. Rodrigues, J. G. Leprince and W. M. Palin, *Int. J. Adhes. Adhes.*, 2016, **69**, 58–71.
110 K. Bazaka, M. V. Jacob, R. J. Crawford and E. P. Ivanova, *Acta Biomater.*, 2011, **7**, 2015–2028.
111 K. A. Whitehead, J. Colligon and J. Verran, *Colloids Surf., B*, 2005, **41**, 129–138.
112 A. Roguska, M. Pisarek, A. Belcarz, L. Marcon, M. Holdynski, M. Andrzejczuk and M. Janik-Czachor, *Appl. Surf. Sci.*, 2016, **388**(Part B), 775–785.
113 H. Li, Q. Cui, B. Feng, J. Wang, X. Lu and J. Weng, *Appl. Surf. Sci.*, 2013, **284**, 179–183.
114 S. D. Puckett, E. Taylor, T. Raimondo and T. J. Webster, *Biomaterials*, 2010, **31**, 706–713.
115 S. Kang, M. Pinault, L. D. Pfefferle and M. Elimelech, *Langmuir*, 2007, **23**, 8670–8673.
116 R. Breaker, *Caries Res.*, 2012, **46**, 78–81.
117 R. E. Marquis, *Can. J. Microbiol.*, 1995, **41**, 955–964.
118 J. Liu, S. C. Rawlinson, R. G. Hill and F. Fortune, *Dent. Mater.*, 2016, **32**, e221–e237.

 This journal is © The Royal Society of Chemistry 2017